Check for updates

JGR Oceans

RESEARCH ARTICLE
10.1029/2026JC024425

Enhanced Southern Ocean O_2 Uptake Due To Bubble-Mediated Gas Exchange Revealed by Climate Model Simulations

Yongqi Wang[1], Changyu Li[1,2], Jianping Huang[1], Lei Ding[3], Xiaoyue Liu[4], Dongliang Han[1], and Ning Huang[2]

[1]Collaborative Innovation Center for Western Ecological Safety, College of Atmospheric Sciences, Lanzhou University, Lanzhou, China, [2]College of Civil Engineering and Mechanics, Lanzhou University, Lanzhou, China, [3]Institute of Disaster Prevention, Beijing, China, [4]Saw Swee Hock School of Public Health, National University of Singapore, Singapore

Abstract Despite advances in understanding the ocean oxygen cycle, climate models continue to show regionally varying discrepancies from O_2 distributions, reflecting incomplete representation of the biological and physical processes controlling ocean oxygen. Air-sea O_2 flux—a key driver of oceanic oxygen variability—remains underconstrained in climate models, with bubble-mediated exchange emerging as a potential missing mechanism. Here we integrate a novel bubble-mediated parameterization into the Community Earth System Model and assess its impact on Southern Ocean O_2 exchange. Including bubble injection increases annual Southern Ocean O_2 uptake by 13%–19%, depending on the prescribed bubble strength. The moderately scaled configuration (BUB-0.3) reduces the near-surface $\Delta[O_2]$ model-observation RMSE in three of the four Southern Ocean regions, with the largest improvement, approximately 34%, occurring in the Subantarctic Zone. In Pacific Subantarctic Mode Water, BUB-0.3 reduces the distributional mismatch with BGC-Argo+ observations by 73%, whereas BUB-1.0 increases the mismatch by 41%. Machine-learning attribution indicates that mixed-layer depth remains the leading predictor of nonthermal O_2 flux variability, while the relative importance and nonlinear influence of wind speed increase when bubble pathways are represented. Our results highlight the importance of bubble-mediated transfer in refining climate models and elucidating the Southern Ocean's capacity as a dynamic oxygen sink, offering a mechanistic advance toward resolving longstanding discrepancies in global marine oxygen cycling.

Plain Language Summary Oxygen in the ocean supports marine life and helps scientists understand how the ocean responds to climate change. However, most climate models calculate the exchange of oxygen between the ocean and the atmosphere without considering bubbles created by breaking waves. In this study, we added a bubble-based gas exchange process into a climate model and tested its impact in the Southern Ocean, a region known for strong winds and large oxygen uptake. Including bubbles increased the simulated Southern Ocean oxygen uptake by about 13%–19%. A moderate representation of bubble effects generally agreed better with oxygen measurements from autonomous profiling floats, both near the ocean surface and in recently formed deeper waters, whereas a stronger representation often added too much oxygen. Mixed-layer depth remained the main predictor of oxygen exchange, but wind speed became more influential and nonlinear when bubble processes were represented. These findings highlight that bubble processes, often neglected in climate models, play a key role in accurately simulating how the ocean takes up oxygen.

Key Points:

- A bubble-mediated parameterization for air-sea O_2 flux was integrated into a climate model in this study
- Including bubble injection increases Southern Ocean O_2 uptake by up to 20%, depending on the prescribed bubble strength
- Machine-learning attribution suggests a nonlinear amplification of wind-speed influence under bubble-enabled schemes

Supporting Information:

Supporting Information may be found in the online version of this article.

Correspondence to:

C. Li,
lichy2013@lzu.edu.cn

Citation:

Wang, Y., Li, C., Huang, J., Ding, L., Liu, X., Han, D., & Huang, N. (2026). Enhanced Southern Ocean O_2 uptake due to bubble-mediated gas exchange revealed by climate model simulations. *Journal of Geophysical Research: Oceans*, *131*, e2026JC024425. https://doi.org/10.1029/2026JC024425

Received 13 APR 2026
Accepted 11 SEP 2026

Author Contributions:

Conceptualization: Changyu Li, Jianping Huang
Data curation: Yongqi Wang
Formal analysis: Yongqi Wang
Investigation: Yongqi Wang
Methodology: Yongqi Wang, Changyu Li
Project administration: Jianping Huang
Resources: Jianping Huang
Supervision: Jianping Huang, Dongliang Han
Validation: Changyu Li, Lei Ding, Xiaoyue Liu, Ning Huang
Visualization: Yongqi Wang
Writing – original draft: Yongqi Wang
Writing – review & editing: Yongqi Wang, Changyu Li, Lei Ding, Xiaoyue Liu, Dongliang Han, Ning Huang

© 2026 American Geophysical Union. All rights reserved, including rights for text and data mining and training of artificial intelligence technologies or similar technologies.

1. Introduction

The concentration of dissolved oxygen (O_2) in the ocean is critical for diversified chemical and biological processes, which structure diversifying marine biota and ecosystems (Huang et al., 2021; Petsch, 2013; Reinhard et al., 2016). Its distribution and evolution could provide important information about ocean circulation, marine biological productivity, carbon uptake as well as the heat and mass transit in the ocean (Bushinsky & Emerson, 2015; Huang et al., 2021; Keeling & Garcia, 2002; Li et al., 2021; Najjar et al., 2007; Resplandy et al., 2016), making O_2 a useful indicator of coupled physical and biogeochemical processes in the Earth system. Recent studies have highlighted the significant role of ocean heat content and deep-ocean heat uptake in influencing climate variability and ocean circulation patterns under climate change (Chen & Tung, 2014; Cheng et al., 2017). These changes in ocean heat storage can further affect marine biogeochemical cycles, including oxygen solubility and distribution (Bopp et al., 2013; Li et al., 2020). Significant losses of global oceanic O_2 content have been

observed since at least the middle of the 20th century and are considered a consequence of warming-induced changes in oxygen solubility and ocean circulation (Long et al., 2016; Oschlies, 2021). The scale of this deoxygenation ranges from the relatively small regions of coastal waters to vast areas of open ocean (Breitburg et al., 2018). In particular, the Southern Ocean is reported as the region where one of the largest O_2 change occurs (Matear et al., 2000; Schmidtko et al., 2017).

Oceanic O_2 distributions arise from the interplay of physical and biogeochemical processes across multiple scales. At the surface, O_2 concentrations are primarily governed by temperature-dependent solubility and wind-driven air-sea exchange, while interior O_2 reflects the balance between ventilation, horizontal circulation, and remineralization of organic matter (Keeling et al., 2010; Oschlies et al., 2018). Net ingassing typically occurs under cooling or enhanced vertical mixing, which lowers surface saturation, whereas warming and photosynthetic production promote supersaturation and outgassing. These diverse processes collectively make O_2 one of the most informative indicators of coupled physical and biogeochemical variability in the Earth system.

Although substantial progress has been made in understanding the ocean oxygen cycle, both Earth system simulations and observation-based reconstructions remain uncertain. Many models underestimate observed O_2 variability or fail to reproduce regional deoxygenation patterns (Frölicher et al., 2016; Stramma et al., 2012), while at the same time observationally based estimates are limited by the sparse and irregular distribution of historical O_2 measurements and the need to interpolate them onto continuous fields. Recent studies have shown that different mapping and gap-filling approaches can substantially affect regional O_2 patterns, seasonal cycles, and long-term trends, particularly in poorly sampled regions such as the Southern Ocean (Du et al., 2026; Ito et al., 2024, 2025). On the modeling side, discrepancies may arise from biases in sea-ice cover, unresolved transport pathways, vertical mixing, or missing biogeochemical feedbacks (Nevison et al., 2015; Oschlies et al., 2018). A further source of uncertainty lies in the parameterization of air-sea O_2 fluxes, which directly links atmospheric forcing, surface-ocean conditions, and interior O_2 budgets (Eddebbar et al., 2017; Morgan et al., 2019). Because mass conservation constrains the global net air-sea O_2 flux through its coupling to long-term changes in oceanic O_2 inventory and interior biogeochemical sources and sinks (R. E. Keeling et al., 2010), inaccuracies in flux parameterizations can strongly influence modeled O_2 dynamics.

Currently the most widely used parameterization for air-sea O_2 flux in current climate models (such as models in Coupled Model Intercomparison Project Phase 6, CMIP6) is generally derived from Wanninkhof (1992), Wanninkhof (2014), which is based on the concept of molecular diffusion across the sea-surface boundary layer and does not explicitly include bubble flux terms (Orr et al., 2017). However, breaking waves entrain bubbles that can substantially enhance gas transfer and inject atmospheric O_2 directly into the mixed layer, leading to near-surface supersaturation and modifying both the magnitude and direction of air-sea O_2 fluxes (Deike et al., 2025; Liang et al., 2013; Liss & Merlivat, 1986; Svein et al., 2010). Recent observational evidence further supports the importance of bubble pathways: eddy-covariance measurements of air-sea CO_2 exchange provide direct field evidence that bubble-mediated transfer can be substantial under strong winds and may be asymmetric between invasion and evasion, consistent with theoretical expectations for bubble processes (Dong et al., 2024, 2025). In addition, independent constraints from inert-gas disequilibria—such as N_2/Ar and noble-gas supersaturation—have been widely used to diagnose and calibrate bubble injection in the surface ocean (Emerson & Bushinsky, 2016; Stanley et al., 2009). For a relatively insoluble gas such as O_2, these bubble-mediated processes become particularly important in high-wind regions, where frequent storms and intense wave breaking prevail, such as the Southern Ocean. The lack of descriptions regarding gas transfer associated with collapsing bubbles in these models may lead to significant biases in assessing the ocean oxygen cycle's response to climate change (Atamanchuk et al., 2020).

Recent studies have begun to incorporate physically based bubble-mediated gas exchange into ocean models. Deike et al. (2025) developed an observation-constrained wind-wave-bubble formulation that explicitly separates nonbreaking exchange, symmetric bubble exchange, and asymmetric bubble injection. When implemented in a global ocean biogeochemical model, this formulation substantially modified simulated air-sea O_2 fluxes. Building on this framework, Rustogi et al. (2026) further demonstrated that accounting for waves and bubbles improved the representation of oxygen saturation in several mode- and deep-water formation regions, reducing model-BGC-Argo+ discrepancies by approximately 70%–90%. These studies provide strong evidence for the importance of asymmetric bubble exchange, but both were conducted using ocean-only modeling frameworks. It therefore remains unclear whether comparable improvements emerge in a fully coupled Earth system model, in which

21699291, 2026, 9, Downloaded from https://agupubs.onlinelibrary.wiley.com/doi/10.1029/2026JC024425 by Jianping Huang - Lanzhou University , Wiley Online Library on [12/11/2026]. See the Terms and Conditions (https://onlinelibrary.wiley.com/terms-and-conditions) on Wiley Online Library for rules of use; OA articles are governed by the applicable Creative Commons License

winds, ocean circulation, vertical mixing, and sea ice evolve interactively, and how sensitive these improvements are to the formulation and magnitude of the bubble contribution.

The Southern Ocean plays a disproportionate role in global O_2 cycling due to its strong westerly winds, intense upwelling of O_2-poor deep waters, and deep winter mixed layers that ventilate mode and intermediate waters (Deike et al., 2025; Sallée et al., 2013; Talley, 2013). Seasonal sea-ice formation and melt, combined with highly variable primary production, create pronounced cycles of undersaturation in winter and localized supersaturation in summer. These dynamic conditions, coupled with persistently high wind speeds, make the Southern Ocean an ideal region for assessing the influence of bubble-mediated processes on air-sea O_2 exchange.

In this study, we implement the bubble-mediated gas-exchange parameterization of Liang et al. (2013) in the Community Earth System Model (CESM, version 2.1.3) and conduct three parallel historical simulations (1940–2014) with varying gas-exchange schemes. We further evaluate the simulations against both near-surface BGC-Argo observations and oxygen properties in Pacific Subantarctic Mode Water (PSAMW), allowing us to assess whether bubble-driven surface uptake is reflected in newly ventilated waters. By comparing the two bubble strengths with recent wind-wave-bubble studies, we examine not only whether asymmetric bubble exchange improves modeled O_2, but also how strongly its magnitude must be observationally constrained in a fully coupled climate model.

2. Data and Methods

2.1. Air-Sea O_2 Flux Parameterizations

2.1.1. The Diffusion-Only Scheme

The most widely used parameterization for air-sea O_2 flux in the climate models is generally derived from (Wanninkhof, 1992), and recently revisited in (Wanninkhof, 2014), which is based on the concept of molecular diffusion across the sea-surface boundary layer and does not explicitly include bubble flux terms:

$$F_{\mathrm{air-sea}} = -k\left([\mathrm{O_2}]_{\mathrm{sat}} - [\mathrm{O_2}]\right)\left(1 - \gamma_{\mathrm{ice}}\right) \tag{1}$$

where $F_{\mathrm{air-sea}}$ is the air-sea O_2 flux (mol m^{-2} s^{-1}). Throughout this study, $F_{\mathrm{air-sea}}$ is defined as positive from the ocean to the atmosphere (outgassing) and negative from the atmosphere into the ocean (ocean uptake or ingassing). k is the mass transfer coefficient for surface air-sea transfer (m s^{-1}), $[O_2]$ is the oxygen concentration in seawater (mol m^{-3}), $[O_2]_{\mathrm{sat}}$ is the saturation concentration derived from (Garcia & Gordon, 1992), and γ_{ice} is the fractional sea-ice coverage (dimensionless, 0–1). The transfer coefficient k could be written as:

$$k = 6.97 \times 10^{-7} U_{10}^2 \left(\frac{Sc_{\mathrm{O2}}}{660}\right)^{-0.5} \tag{2}$$

Here, U_{10} is the 10-m neutral wind speed (m s^{-1}), and Sc_{O2} is the dimensionless Schmidt number for O_2. The empirical coefficient in the Wanninkhof formulation was originally derived and calibrated for CO_2 gas exchange; here, its application to O_2 follows the conventional Schmidt-number scaling using Sc_{O2}.

2.1.2. The Bubble-Mediated Scheme

The bubble-mediated gas flux parameterizations for air-sea flux are currently undergoing development (Deike et al., 2025; Krall et al., 2019; Woolf, 1997). In this study, we adopt the parameterization of Liang et al. (2013). Although several gas-transfer formulations distinguish among different bubble classes, the Liang formulation provides an explicit and relatively straightforward representation of fully collapsing small bubbles and partially dissolving large bubbles using variables readily available in CESM2. In addition, the formulation has been evaluated against noble-gas and N_2/Ar constraints and has previously been applied to Southern Ocean O_2 exchange, facilitating comparison with earlier observationally based studies (Bushinsky et al., 2017; Emerson & Bushinsky, 2016). The bubble-mediated parameterization for air-sea O_2 flux could be formulated as:

$$F_{\mathrm{air-sea}} = \left(F_s + \beta F_c + \beta F_p\right)\left(1 - \gamma_{\mathrm{ice}}\right) \tag{3}$$

21699291, 2026, 9, Downloaded from https://agupubs.onlinelibrary.wiley.com/doi/10.1029/2026JC024425 by Jianping Huang - Lanzhou University , Wiley Online Library on [12/11/2026]. See the Terms and Conditions (https://onlinelibrary.wiley.com/terms-and-conditions) on Wiley Online Library for rules of use; OA articles are governed by the applicable Creative Commons License

21699291, 2026, 9, Downloaded from https://agupubs.onlinelibrary.wiley.com/doi/10.1029/2026JC024425 by Jianping Huang - Lanzhou University , Wiley Online Library on [12/11/2026]. See the Terms and Conditions (https://onlinelibrary.wiley.com/terms-and-conditions) on Wiley Online Library for rules of use; OA articles are governed by the applicable Creative Commons License

The total bubble-mediated air-sea O_2 flux is partitioned into Fs, Fc and Fp, where the subscripts s, c, and p denote surface diffusive exchange, fully collapsing small bubbles, and partially dissolving large bubbles, respectively. A tuning parameter, β, is applied to the model to adjust the contributions of bubble injection (Bushinsky et al., 2017; Emerson et al., 2019; Yang et al., 2017).

The diffusive component F_s could be calculated as:

$$F_s = -1.3 \times 10^{-4} U_a^* \left(\frac{Sc_{O2}}{660}\right)^{-0.5} \left([O_2]_{sat} - [O_2]\right) \tag{4}$$

Here, U_a^* is the air-side friction velocity (m s^{-1}), which is related to the drag coefficient C_d and the 10-m neutral wind speed U_{10} (Large & Pond, 1981; Sullivan et al., 2012):

$$U_a^* = \sqrt{C_d} U_{10} \tag{5}$$

$$C_d = \begin{cases} 0.0012, U_{10} \le 11\ \text{ms}^{-1} \\ (0.49 + 0.065U_{10}) \times 10^{-3}, 11\ \text{ms}^{-1} < U_{10} < 20\ \text{ms}^{-1} \\ 0.0018, U_{10} \ge 20\ \text{ms}^{-1} \end{cases} \tag{6}$$

The small bubbles, which slow buoyant rising velocities, could be trapped in the boundary layer and completely collapse. Its contribution to air-sea O_2 flux could be written as:

$$F_c = -5.56 U_w^{*\,3.86} X_{O_2} \tag{7}$$

where X_{O2} represents the standard mole fraction of O_2 in the atmosphere ($XO_2 = 20.946\%$); U_w^* is the water-side friction velocity (m s^{-1}).

$$U_w^* = 0.034 \sqrt{C_d} U_{10} \tag{8}$$

The large bubbles have a relatively fast rising speed, which could only partially dissolve in seawater. Its effect on O_2 exchange could be formulated as:

$$F_p = -5.5 U_w^{*\,2.76} \left(\frac{Sc_{O2}}{660}\right)^{-0.67} \left((1 + \Delta P)[O_2]_{sat} - [O_2]\right) \tag{9}$$

where ΔP represents the supersaturation of the O_2 concentration by partially dissolved bubbles

$$\Delta P = 1.52 U_w^{*\,1.06} \tag{10}$$

2.2. Offline Idealized Comparison Between the Two Parameterizations

To isolate the instantaneous behavior of the two gas-exchange formulations, we performed an offline diagnostic calculation independent of the coupled CESM simulations (Figure 1). The two parameterizations were evaluated over prescribed ranges of 10-m wind speed and surface-ocean O_2 disequilibrium while sea surface temperature, salinity, atmospheric pressure, and relative humidity were held fixed at 5°C, 35 PSU, 1 atm, and 85%, respectively. Because the environmental conditions and surface O_2 concentrations were prescribed, this idealized calculation does not include feedbacks associated with the evolution of ocean O_2, circulation, mixed-layer dynamics, biological processes, sea ice, or atmosphere-ocean coupling. Its purpose is therefore to illustrate the instantaneous mathematical response of each parameterization rather than the equilibrated response of the coupled climate system. Surface O_2 disequilibrium is defined as $\Delta[O_2] = [O_2] - [O_2]_{sat}$, with negative and positive values indicating undersaturation and supersaturation, respectively.

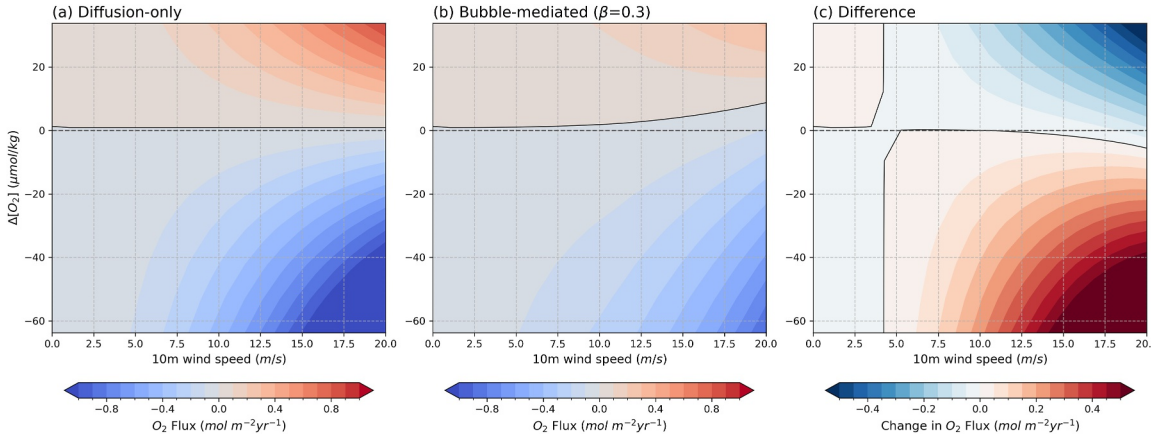


Figure 1. Offline idealized comparison of air-sea O_2 flux calculated using the diffusion-only and bubble-mediated parameterizations as functions of 10-m wind speed and surface O_2 concentration difference ($\Delta[O_2] = [O_2] - [O_2]_{sat}$). Negative $\Delta[O_2]$ represents undersaturated surface water, whereas positive $\Delta[O_2]$ represents supersaturated water. The vertical dashed line marks thermodynamic saturation ($\Delta[O_2] = 0$). Positive air-sea O_2 flux denotes transfer from the ocean to the atmosphere (outgassing), and negative flux denotes transfer from the atmosphere into the ocean (uptake). The calculations assume a fixed sea surface temperature of 5°C, salinity of 35 PSU, atmospheric pressure of 1 atm, and relative humidity of 85%. Panel (c) shows $F_{BUB} - F_{DIFF}$; negative differences indicate enhanced ocean uptake or reduced outgassing under the bubble-mediated scheme, whereas positive differences indicate enhanced outgassing or reduced uptake. The color-bar range in panel (c) differs from those in panels (a) and (b) to highlight differences between the parameterizations.

Both parameterizations generally produce ocean uptake under undersaturated conditions and outgassing under supersaturated conditions, with the magnitude of exchange increasing with wind speed. However, including bubble-mediated exchange modifies both the magnitude of the flux and the $\Delta[O_2]$ at which the total flux changes sign. In particular, the inward bubble flux can offset diffusive outgassing, allowing net ocean uptake to persist under slightly supersaturated conditions. The Wanninkhof transfer coefficient increases approximately with U_{10}^2, whereas the surface-diffusive component in the Liang formulation increases more slowly with wind speed through $\sqrt{C_d}U_{10}$. As a result, under strongly undersaturated and high-wind conditions, the difference in diffusive uptake between the two formulations can exceed the additional inward flux contributed by the scaled bubble terms ($\beta = 0.3$), resulting in weaker total uptake under the bubble-mediated formulation.

2.3. Model Description and Numerical Experiments

The simulations in this study are based on the CESM version 2.1.3 (CESM2), developed by the National Center for Atmospheric Research. CESM2 is an open-source, fully-coupled, community and global climate model that consists of ocean (POP2), atmosphere (CAM6), land (CLM5), land-ice (CISM2.1), sea-ice (CICE5) and river (MOSART) components (Danabasoglu et al., 2012; Hurrell et al., 2013; Lawrence et al., 2019; Li et al., 2013; Turner & Hunke, 2015), providing state-of-the-art computer simulations of the Earth's climate states (Danabasoglu et al., 2020). The simulations were initialized from a spun-up, fully coupled CESM2 pre-industrial control simulation. All experiments used the BHIST component set and were subsequently integrated from 1850 to 2014 following the CMIP6 historical forcing protocol, including prescribed greenhouse gases, anthropogenic and natural aerosols, volcanic forcing, solar variability, and land-use change (Eyring et al., 2016).

The coupled model provides internally consistent surface forcing and ocean circulation needed for air-sea exchange, including (a) atmosphere-to-ocean fluxes of momentum, heat, and freshwater derived from CAM6 near-surface state and winds; (b) ocean mixed-layer dynamics and vertical transport/mixing in POP2 (e.g., surface boundary layer turbulence and interior diapycnal mixing), which regulate near-surface tracer gradients; (c) parameterized mesoscale eddy effects and isopycnal tracer mixing; and (d) dynamic-thermodynamic sea ice in CICE5 that modulates the open-water fraction and thus the area available for gas exchange. All experiments are performed at the same model resolution (gx1v7 grid, ~1°), vertical discretization (60 levels, max depth ~5,500 m), and component time steps (3,600 s).

Ocean biogeochemistry is simulated with the Marine Biogeochemistry Library (MARBL), an updated implementation of the Biogeochemical Elemental Cycling model (Moore et al., 2004, 2013). In the CESM2 MARBL configuration, the marine ecosystem is represented with multiple plankton functional types and prognostic

21699291, 2026, 9, Downloaded from https://agupubs.onlinelibrary.wiley.com/doi/10.1029/2026JC024425 by Jianping Huang - Lanzhou University , Wiley Online Library on [12/11/2026]. See the Terms and Conditions (https://onlinelibrary.wiley.com/terms-and-conditions) on Wiley Online Library for rules of use; OA articles are governed by the applicable Creative Commons License

21699291, 2026, 9, Downloaded from https://agupubs.onlinelibrary.wiley.com/doi/10.1029/2026JC024425 by Jianping Huang - Lanzhou University , Wiley Online Library on [12/11/2026]. See the Terms and Conditions (https://onlinelibrary.wiley.com/terms-and-conditions) on Wiley Online Library for rules of use; OA articles are governed by the applicable Creative Commons License

biogeochemical tracers that include dissolved O_2 and key nutrient and carbon-system tracers. Oxygen is produced and consumed through biological source-sink processes (e.g., net community production and remineralization/respiration) and is transported by the same POP2 advection and mixing operators as temperature and salinity, ensuring consistent coupling between circulation and biogeochemical distributions. Air-sea O_2 fluxes are computed within MARBL and applied as a surface boundary flux to the ocean O_2 tracer; fluxes are reduced in the presence of sea ice by scaling with open-water fraction using sea-ice concentration from CICE5.

To investigate the role of bubble injection in air-sea O_2 exchange, we conducted three parallel experiments with different parameterizations for the air-sea O_2 flux. First, we performed a simulation using the non-bubble scheme of Wanninkhof (1992), Wanninkhof (2014), representing the original formulation in CESM that does not include explicit bubble-injection terms; we refer to this configuration as the diffusion-only scheme (DIFF). Second, we implemented the bubble-mediated gas flux parameterization of (Liang et al., 2013), which explicitly partitions the total flux into a diffusive component (Fs) and bubble-mediated components associated with small, fully dissolving bubbles (Fc) and large, partially dissolving bubbles (Fp). Two bubble strengths were examined: (a) a strong-bubble configuration with $\beta = 1.0$ (BUB-1.0), corresponding to the original formulation of (Liang et al., 2013), and (b) a moderately scaled bubble configuration with $\beta = 0.3$ (BUB-0.3), an observationally tuned value for the Southern Ocean following Bushinsky et al. (2017).

Because different gas transfer formulations modify the surface O_2 boundary flux from the beginning of the historical integration, an initial adjustment of the ocean O_2 inventory is expected. To minimize the influence of this transient adjustment, we focus our analysis on the later historical period (2000–2014). Unless otherwise specified, differences between the bubble-mediated and diffusion-only experiments are calculated as $\Delta F = F_{\mathrm{BUB}} - F_{\mathrm{DIFF}}$. Positive ΔF denotes a shift in the flux toward the atmosphere, representing either enhanced outgassing or reduced ocean uptake, whereas negative ΔF denotes a shift toward the ocean, representing either enhanced uptake or reduced outgassing.

2.4. Southern Ocean Regional Division

Based on climatological averages of temperature and salinity, Bushinsky et al. (2017) divide the Southern Ocean into four regions: the Subtropical Zone (STZ), the Subantarctic Zone (SAZ), the Polar Frontal-Antarctic Zone (PAZ), and the Seasonal Ice Zone (SIZ) (Figure 2a). Each region exhibits distinct seasonal patterns in both biogeochemical and physical characteristics. The STZ is the northernmost region of the Southern Ocean, extending from 30°S to the Subtropical Front. This region is characterized by warm, saline waters with a shallow mixed layer and is largely influenced by the subtropical circulation. The SAZ, situated between the Subtropical and Subantarctic Fronts, is characterized by a deep winter mixed layer and the largest seasonal amplitude in nitrate concentrations. The PAZ, located between the Subantarctic Front and the SIZ, is a critical region for oxygen uptake. Strong turbulence and high wind speeds make bubble-mediated processes particularly important in this region. The SIZ consists of waters seasonally covered by sea ice, limits light availability for photosynthesis and restricts air-sea gas exchange. This region has the shallowest mixed layers of the four regions. It is completely covered by sea ice in winter, with the ice melting and exposing the ocean surface in summer (Orsi et al., 1995; Roemmich & Gilson, 2009).

2.5. BGC-Argo+ Data and Model-Observation Collocation

We evaluate the simulated oxygen fields using quality-controlled observations from the BGC-Argo+ data set (Bushinsky, 2025), which provides harmonized biogeochemical Argo profiles together with secondary quality control and derived hydrographic variables. We selected all available profiles located south of 30°S during 2004–2014, corresponding to the period shared by the observations and the CESM simulations. Dissolved oxygen, temperature, salinity, pressure, and associated quality-control information were obtained from the adjusted BGC-Argo+ variables. Samples that did not pass the recommended quality-control criteria or contained missing values were excluded from the analysis. CESM dissolved oxygen, originally expressed in mmol m^{-3}, was converted to μmol kg^{-1} using the corresponding model seawater density before comparison with BGC-Argo+.

For the near-surface evaluation, observations within the upper 0–10 dbar of each profile were averaged to represent the oxygen state immediately below the air-sea interface. This depth interval is comparable to the uppermost CESM ocean layer (5 m). Profiles without valid oxygen, temperature, and salinity measurements within this interval were excluded. A small float-shipboard oxygen offset at depths of approximately

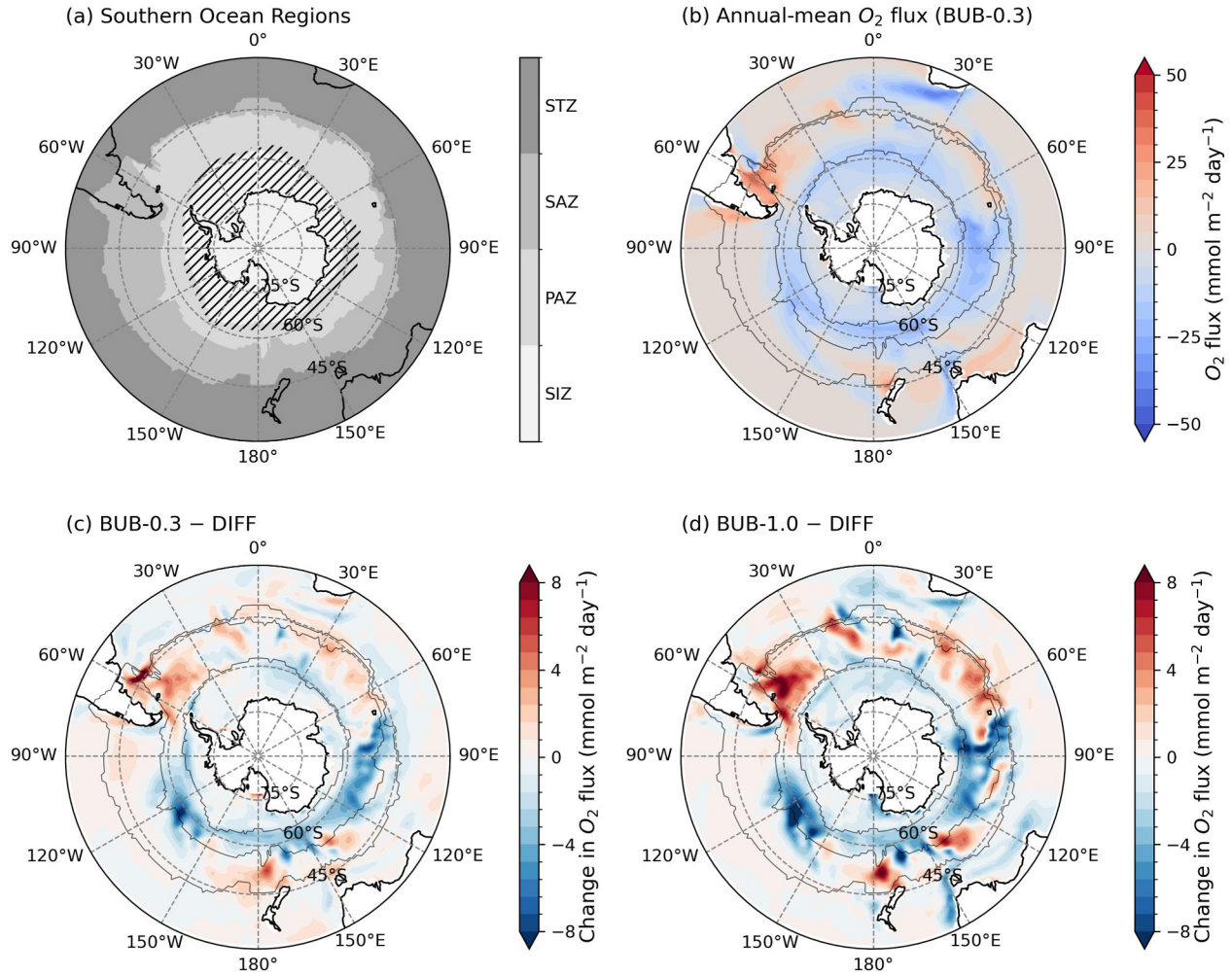


Figure 2. (a) Four regions defined in the Southern Ocean: Subtropical Zone (STZ), Subantarctic Zone (SAZ), Polar Frontal-Antarctic Zone (PAZ) and seasonal ice zone, shown by different grey shades. Hatching indicates the climatological maximum sea-ice extent, defined as regions with sea-ice concentration ≥15% during the month of maximum climatological sea-ice area (October) over 2000–2014. (b) Spatial distribution of the annual mean air-sea O_2 flux under the BUB-0.3 scheme. (c) and (d) depict the differences in air-sea O_2 fluxes between the BUB schemes (BUB-0.3 and BUB-1.0, respectively) and the DIFF scheme. Positive differences indicate enhanced outgassing or reduced ocean uptake relative to DIFF, whereas negative differences indicate enhanced ocean uptake or reduced outgassing.

1,450–2,000 dbar has previously been reported (Bushinsky et al., 2025). Because the present near-surface evaluation uses adjusted O_2 observations within the upper 0–10 dbar, no additional deep-water bias correction was applied.

We use near-surface $\Delta[O_2]$ as the primary model-evaluation metric because it is directly relevant to air-sea gas exchange. Evaluating the model against $\Delta[O_2]$, rather than against observation-based air-sea flux estimates, also avoids prescribing a gas-exchange formulation in the observational benchmark. Note that while Bushinsky et al. (2017) previously estimated Southern Ocean air-sea O2 fluxes using these BGC-Argo data, their estimates depend on an assumed gas-exchange formulation with bubble scaling ($\beta = 0.3$; Liang et al., 2013). To keep our evaluation independent of any prescribed gas-exchange parameterization, we benchmark simulations against float-derived surface $\Delta[O_2]$ rather than their flux estimates. For each observed and modeled profile, we compute the saturation concentration $[O_2]_{sat}$ from in situ temperature and salinity using the solubility formulation of Garcia and Gordon (1992).

The near-surface comparison does not constitute an evaluation of the complete ocean oxygen inventory. Surface $\Delta[O_2]$ does not directly constrain subsurface oxygen concentrations, vertically integrated oxygen storage, or the subsequent transport of newly absorbed oxygen into mode and intermediate waters. The analysis should therefore

21699291, 2026, 9, Downloaded from https://agupubs.onlinelibrary.wiley.com/doi/10.1029/2026JC024425 by Jianping Huang - Lanzhou University , Wiley Online Library on [12/11/2026]. See the Terms and Conditions (https://onlinelibrary.wiley.com/terms-and-conditions) on Wiley Online Library for rules of use; OA articles are governed by the applicable Creative Commons License

21699291, 2026, 9, Downloaded from https://agupubs.onlinelibrary.wiley.com/doi/10.1029/2026JC024425 by Jianping Huang - Lanzhou University , Wiley Online Library on [12/11/2026]. See the Terms and Conditions (https://onlinelibrary.wiley.com/terms-and-conditions) on Wiley Online Library for rules of use; OA articles are governed by the applicable Creative Commons License

be interpreted specifically as an evaluation of the simulated near-surface $\Delta[O_2]$ associated with the air-sea boundary condition.

To assess whether the influence of bubble-mediated surface exchange is retained in newly ventilated waters, we further evaluated dissolved O_2 in Pacific Subantarctic Mode Water (PSAMW). BGC-Argo+ profiles were restricted to the Pacific sector between 170°E and 70°W and between 64°S and 45°S, and only profiles collected during August and September were retained. Profiles were additionally required to have a mixed-layer depth of at least 200 m, representing conditions associated with deep winter ventilation. Within each retained profile, samples were selected when their potential density (σ_θ) anomaly satisfied $26.8 \leq \sigma_\theta \leq 27.05$ kg m^{-3}, and their depths were at least 20 m above the base of the mixed layer ($z \leq$ MLD-20 m). Samples with missing or invalid dissolved oxygen, temperature, salinity, or potential-density values were excluded.

For each retained profile, CESM temperature, salinity, density, and dissolved oxygen from the corresponding calendar month and nearest model grid cell were vertically interpolated to the BGC-Argo+ sampling depths. The median of all selected PSAMW samples was calculated separately for each observed and modeled profile, providing one representative value per profile. Distributional agreement between the simulations and BGC-Argo+ observations was quantified using the one-dimensional Earth Mover's Distance, equivalent to the first Wasserstein distance,

$$D = \int_{-\infty}^{+\infty} |F_{model}(x) - F_{obs}(x)|\, dx \tag{11}$$

where $F_{model}(x)$ and $F_{obs}(x)$ are the empirical cumulative distribution functions. Smaller D values indicate closer agreement between the modeled and observed distributions.

2.6. Thermal-Nonthermal Decomposition and Machine-Learning Attribution

Oxygen solubility is strongly dependent on temperature. To isolate the biological and dynamical mechanisms controlling air-sea oxygen exchange from thermodynamic effects, the total O_2 flux (F_{total}) was separated into thermal ($F_{thermal}$) and non-thermal ($F_{nonthermal}$) components. Following the approach of Keeling et al. (1993), assuming instantaneous equilibration with sea surface temperature changes, $F_{thermal}$ can be calculated as:

$$F_{thermal} = \frac{\partial [O_2]_{sat}}{\partial T} \frac{Q}{C_p} \tag{12}$$

where $\partial[O_2]_{sat}/\partial T$ (mol kg^{-1} K^{-1}) is the temperature derivative of oxygen solubility, Q (J m^{-2} s^{-1}) is the total heat flux, and Cp (J m^{-3} K^{-1}) is the volumetric heat capacity of seawater. The non-thermal component is then defined as the residual $F_{nonthermal} = F_{total} - F_{thermal}$.

To evaluate the drivers of $F_{nonthermal}$, we constructed regression models using the Light Gradient Boosting Machine algorithm (LightGBM; Ke et al., 2017). The target variable was $F_{nonthermal}$ and the predictors were (a) Mixed Layer Depth (MLD), representing vertical mixing, entrainment, and ventilation potential; (b) Gross Oxygen Production, integrated over the mixed layer, representing photosynthetic O_2 production; and (c) 10-m wind speed, representing turbulent transfer and bubble-mediated gas exchange. Each sample represented one monthly model grid cell during 2000–2014, and samples containing missing or nonfinite values in either the target or predictors were excluded.

Separate LightGBM models were trained for each of the four Southern Ocean regions and each gas-exchange configuration, resulting in 12 independently fitted models. To quantitatively assess model skill, we compute standard statistical metrics, including bias and root-mean-square error (RMSE), as defined below:

$$RMSE = \sqrt{\frac{1}{N}\sum (F_{Model,i} - F_{Float,i})^2} \tag{13}$$

21699291, 2026, 9, Downloaded from https://agupubs.onlinelibrary.wiley.com/doi/10.1029/2026JC024425 by Jianping Huang - Lanzhou University , Wiley Online Library on [12/11/2026]. See the Terms and Conditions (https://onlinelibrary.wiley.com/terms-and-conditions) on Wiley Online Library for rules of use; OA articles are governed by the applicable Creative Commons License

Predictor contributions were quantified using SHapley Additive exPlanations (SHAP; Lundberg & Lee, 2017). SHAP values were calculated using the tree-based explainer for each fitted LightGBM model (Lundberg et al., 2020). Global feature importance was calculated as the mean absolute SHAP value of each predictor across all samples within each regional model. Larger mean absolute SHAP values indicate a greater average contribution to the LightGBM predictions but do not by themselves establish causal relationships.

3. Results

3.1. Characteristics of Air-Sea O_2 Flux in the Southern Ocean

We first examine the spatial distribution of the annual-mean air-sea O_2 flux (Figure 2b, averaged over 2000–2014; see Figure S1 in Supporting Information S1 for other two schemes). The Southern Ocean predominantly exhibits oxygen release at low latitudes and uptake at high latitudes, with pronounced outgassing near South America and significant uptake zones along the Antarctic Circumpolar Current (ACC). Notably, the bubble-mediated anomalies (Figures 2c and 2d) align closely with these net flux patterns, indicating that bubble processes primarily scale up the pre-existing gas exchange rather than reversing its direction. Pronounced positive flux anomalies toward the atmosphere are concentrated in the western subpolar South Atlantic and Indian Ocean sectors. Positive anomalies cover 43.5% and 44.6% of the Southern Ocean area in BUB-0.3 and BUB-1.0, respectively. Within these areas, the area-weighted median anomalies are 0.55 and 0.49 mmol m^{-2} d^{-1}, and the corresponding 95th-percentile values are 2.66 and 4.56 mmol m^{-2} d^{-1}. Negative anomalies, indicating enhanced ocean uptake or reduced outgassing, are concentrated in the eastern subpolar Indian and southern Pacific sectors. Within the ACC belt (~45°S–60°S), where baseline absorption is already strong, the BUB schemes further intensify the oxygen sink. The nearly identical spatial patterns of BUB-0.3 and BUB-1.0 (though BUB-1.0 is more pronounced) indicate that the bubble-mediated contribution is positively correlated with the intensity of the background flux, with the effect peaking in high-wind "storm track" regions. Although seasonal sea ice limits annual-mean gas exchange near the Antarctic margin (Figure 2b), surface O_2 undersaturation is present in all seasons in the high-latitude Southern Ocean (Figure S3 in Supporting Information S1). During ice-free periods, strong winds and the nonlinear bubble response enhance O_2 uptake into these cold, undersaturated waters relative to the DIFF Scheme.

Due to the distinct regional characteristics of air-sea O_2 fluxes in the Southern Ocean, we divided it into four regions as described in Section 2.4. Using O_2 fluxes and the corresponding area of each region, we quantified the annual O_2 flux for each region under different parameterization schemes, as illustrated in Figure 3a. Annual fluxes were first calculated separately for each year during 2000–2014. Unless otherwise stated, values are reported as the 15-year mean ±1 standard error, calculated across the 15 annual-mean fluxes. The sign convention defined in Section 2.1 is retained for spatially integrated fluxes: positive values in Tmol yr^{-1} indicate net outgassing, whereas negative values indicate net ocean uptake. As the northernmost region of the Southern Ocean, the STZ shows an annual average O_2 flux of $+9.5 \pm 1.9$ Tmol yr^{-1} (1 Tmol = 10^{12} mol) under the DIFF Scheme. BUB-0.3 yields a nearly identical flux ($+9.5 \pm 1.9$ Tmol yr^{-1}), whereas BUB-1.0 reduces the outgassing to $+7.2 \pm 2.1$ Tmol yr^{-1}, a decrease of approximately 24.2% relative to DIFF. In the SAZ, the annual mean O_2 flux remains near zero under both the original and new parameterization schemes, with annual fluxes of $+2.4 \pm 1.6$, $+0.4 \pm 1.5$, and $+1.1 \pm 1.5$ Tmol yr^{-1} for DIFF, BUB-0.3, and BUB-1.0, respectively, indicating substantial seasonal compensation in this region. In contrast, the PAZ and SIZ act as the major regional O_2 sinks. In the PAZ, air-sea O_2 flux decreases from -64.6 ± 3.0 Tmol yr^{-1} under DIFF to -72.3 ± 2.4 Tmol yr^{-1} under BUB-0.3 and -74.4 ± 4.1 Tmol yr^{-1} under BUB-1.0, corresponding to increases in uptake magnitude of approximately 11.8% and 15.2%, respectively. Similarly, SIZ air-sea O_2 flux decreases from -34.7 ± 0.7 Tmol yr^{-1} under DIFF to -37.5 ± 0.8 Tmol yr^{-1} under BUB-0.3 and -42.9 ± 1.5 Tmol yr^{-1} under BUB-1.0, representing enhancements of approximately 8.3% and 23.8%. Thus, introducing bubble-mediated exchange leaves the broad regional pattern of Southern Ocean O_2 exchange unchanged but strengthens net uptake primarily in the high-latitude PAZ and SIZ, with the largest regional response occurring in the SIZ under BUB-1.0.

In addition to the regional budgets, we further integrated the air-sea O_2 flux over the entire Southern Ocean (south of 30°S; Figure 3b). The Southern Ocean annual-mean flux decreases from -96.6 ± 4.4 Tmol yr^{-1} under the DIFF scheme to -108.7 ± 4.6 Tmol yr^{-1} under BUB-0.3 and -114.5 ± 6.0 Tmol yr^{-1} under BUB-1.0. These changes correspond to increases in the magnitude of Southern Ocean O_2 uptake of approximately 12.5% and 18.5%, respectively, indicating a robust basin-scale enhancement of O_2 uptake when bubble-mediated exchange is included. For context, Bushinsky et al. (2017) estimated a mean Southern Ocean air-sea O_2 flux of

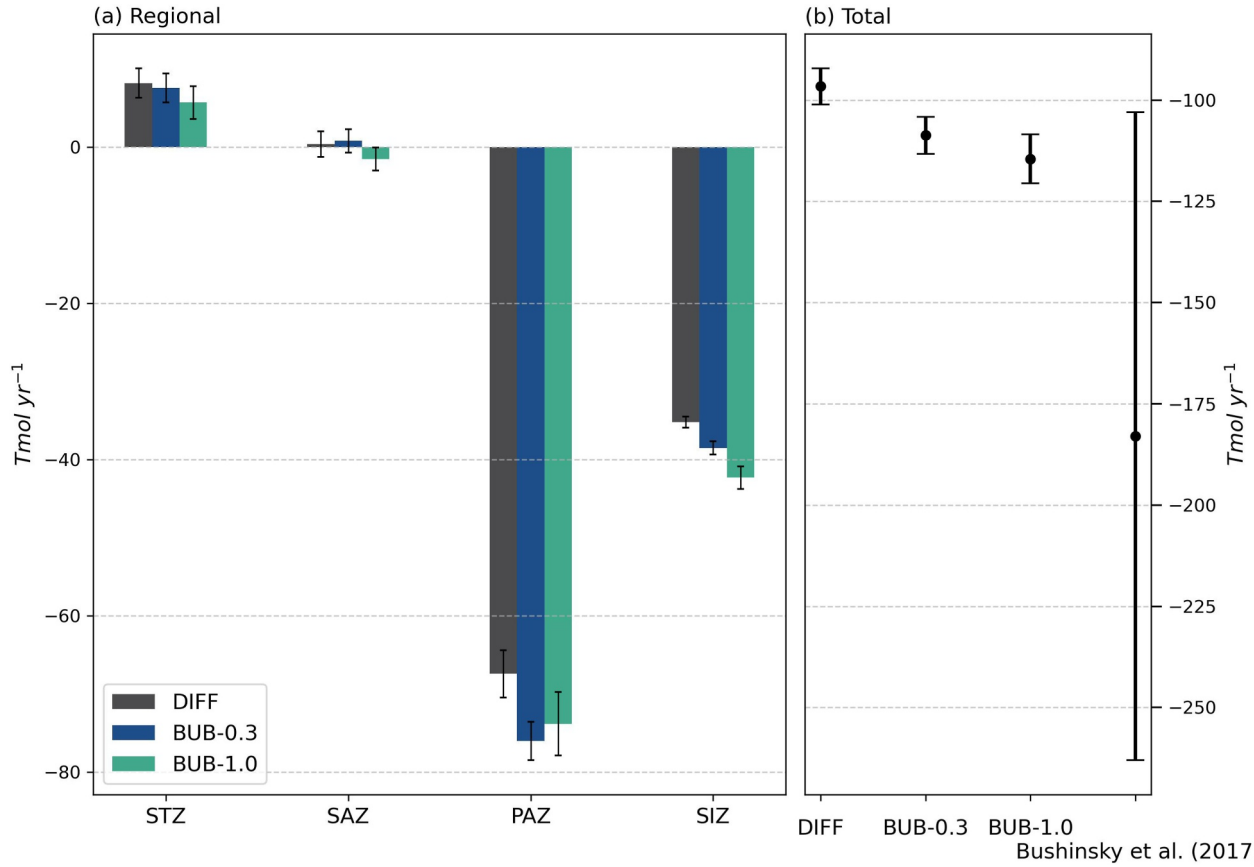


Figure 3. (a) Annual mean air-sea O_2 fluxes across four regions of the Southern Ocean under different parameterization schemes. (b) Annual mean air-sea O_2 fluxes for the entire Southern Ocean (south of 30°S) under different parameterization schemes, with O_2 flux derived from Argo floats. Error bars denote ±1 standard error across years; the Bushinsky et al. (2017) error bar shows the uncertainty reported in that study.

-183 ± 80 Tmol yr^{-1} using float observations collected during 2008–2016. The substantially larger uncertainty reported for this observational estimate is not directly comparable to the standard errors of the simulated fluxes shown in Figure 3. The model standard errors are calculated from 15 spatially integrated annual-mean fluxes over the complete Southern Ocean model grid, for which spatial integration tends to smooth localized and episodic variability. In contrast, the Bushinsky et al. estimate was derived from spatially and temporally discrete profiling-float observations using an assumed gas-exchange formulation and is therefore more sensitive to observational sampling, representativeness, and uncertainties associated with flux estimation. Moreover, their estimate was derived using the (Liang et al., 2013) parameterization with $\beta = 0.29$. We therefore show this observational estimate as contextual information rather than as a directly comparable measure of model uncertainty or an independent criterion for selecting bubble strength.

Furthermore, we analyze the seasonal variability of the air-sea O_2 flux in the Southern Ocean. The spatial distribution of O_2 flux simulated under the BUB-0.3 scheme for different seasons is shown in Figure S2 in Supporting Information S1. A pronounced seasonal cycle is evident across the Southern Ocean, with net oxygen release to the atmosphere during austral summer and net oxygen uptake during winter. During spring and autumn, high-latitude regions (the PAZ and SIZ) show oxygen uptake, whereas the STZ and SAZ tend to exhibit net O_2 outgassing. To further examine regional differences, Figure 4 presents the monthly variations in air-sea O_2 flux across the four Southern Ocean regions under different gas-exchange parameterizations. Despite regional contrasts, all regions share a consistent seasonal phasing, characterized by oxygen uptake in winter and release in summer. At higher latitudes, the transition from summer outgassing to winter uptake occurs earlier, and the return to outgassing is delayed, resulting in an extended uptake period. Although the SIZ experiences the longest uptake season, the PAZ exhibits the largest seasonal amplitude. Specifically, the PAZ absorbs 39.4 ± 0.3 mmol m^{-2} d^{-1} in August and releases 34.1 ± 0.3 mmol m^{-2} d^{-1} in December under the BUB-0.3 scheme.

21699291, 2026, 9, Downloaded from https://agupubs.onlinelibrary.wiley.com/doi/10.1029/2026JC024425 by Jianping Huang - Lanzhou University , Wiley Online Library on [12/11/2026]. See the Terms and Conditions (https://onlinelibrary.wiley.com/terms-and-conditions) on Wiley Online Library for rules of use; OA articles are governed by the applicable Creative Commons License

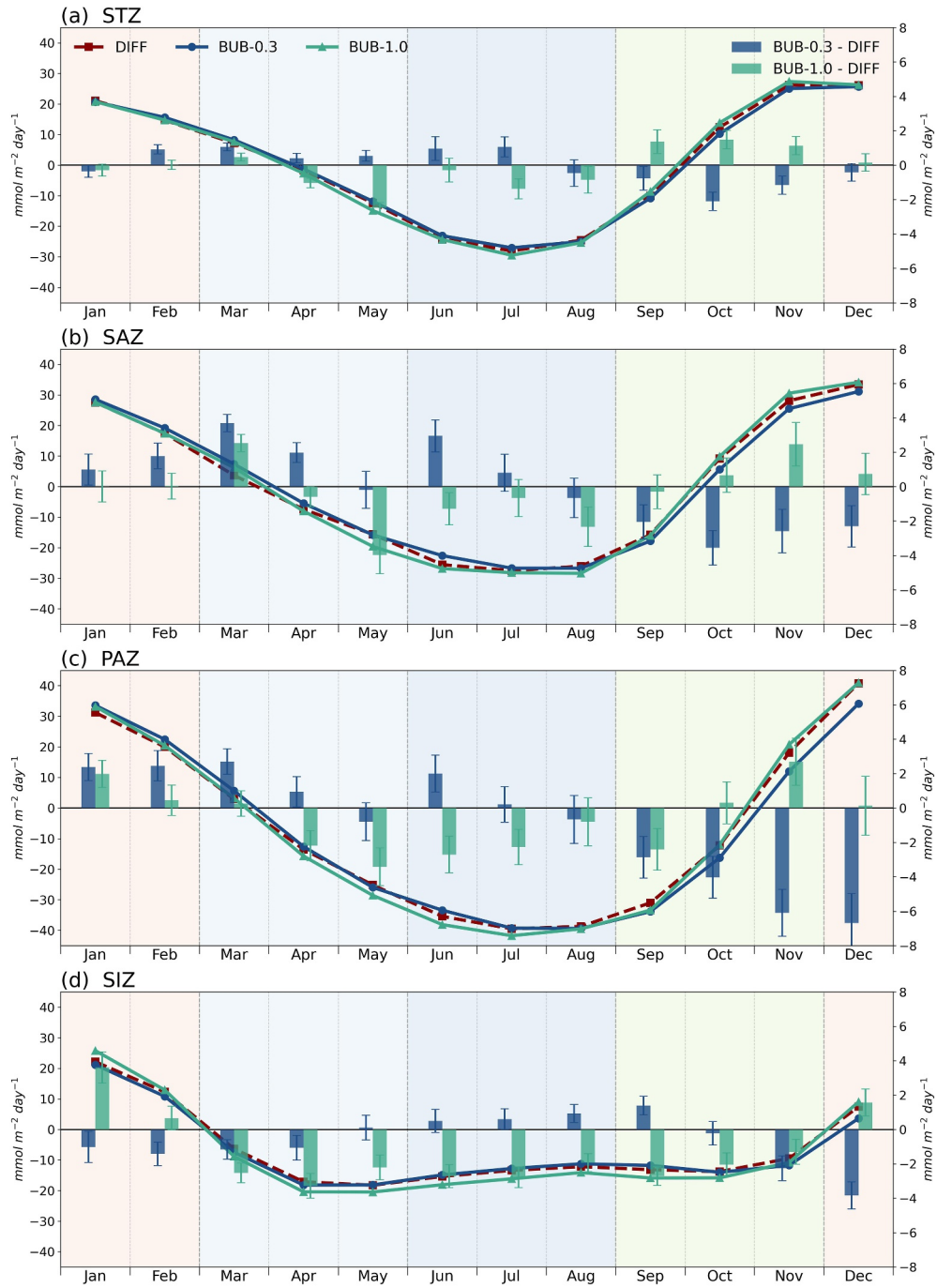


Figure 4. Seasonal cycles of air-sea O_2 flux across four regions of the Southern Ocean (a) the Subtropical Zone (STZ), (b) the Subantarctic Zone (SAZ), (c) the Polar Frontal-Antarctic Zone (PAZ), and (d) the seasonal ice zone (SIZ). Lines show the climatological monthly mean O_2 fluxes under the diffusion-only (DIFF), BUB-0.3, and BUB-1.0 simulations, with values referenced to the left axis. Bars show the corresponding differences between the bubble-mediated and DIFF simulations (BUB-0.3 − DIFF and BUB-1.0 − DIFF), with values referenced to the right axis. Error bars denote ±1 standard error across years. Background shading denotes austral summer (DJF), autumn (MAM), winter (JJA), and spring (SON).

The spatial distribution of the seasonal difference between the BUB and DIFF schemes is presented in Figure 5 (BUB-0.3 – DIFF) and Figure 6 (BUB-1.0 – DIFF). After applying the BUB-0.3 scheme, springtime oxygen uptake increases significantly, with a mean enhancement of 86.87 Tmol yr^{-1} over the Southern Ocean. In contrast, autumn and winter are characterized by a net enhancement of oxygen release to the atmosphere. Under

21699291, 2026, 9, Downloaded from https://agupubs.onlinelibrary.wiley.com/doi/10.1029/2026JC024425 by Jianping Huang - Lanzhou University , Wiley Online Library on [12/11/2026]. See the Terms and Conditions (https://onlinelibrary.wiley.com/terms-and-conditions) on Wiley Online Library for rules of use; OA articles are governed by the applicable Creative Commons License

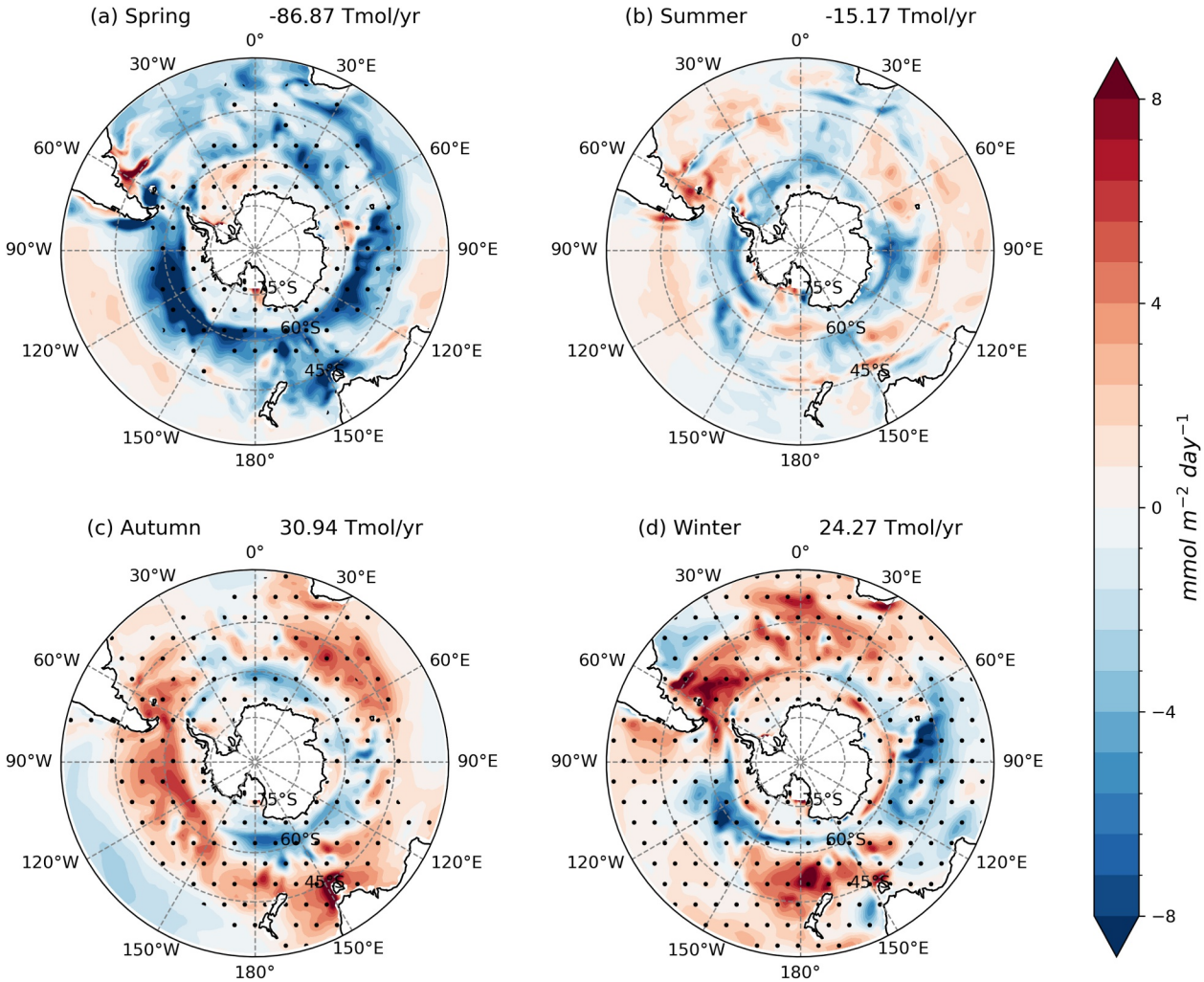


Figure 5. Spatial distribution of the seasonal mean air-sea O_2 flux differences between BUB-0.3 and DIFF. The seasons are defined as follows: spring (September–November), summer (December–February), autumn (March–May) and winter (June–August). Stippling denotes regions where the seasonal-mean air-sea O_2 flux under the DIFF scheme is negative, indicating net oceanic O_2 uptake.

BUB-1.0, the enhancement of O_2 uptake is more pronounced in autumn and winter, with regional area-integrated differences relative to DIFF of −52.97 and −57.25 Tmol yr^{-1}, respectively. In spring and summer, oxygen outgassing is enhanced. Monthly differences between the BUB schemes and the DIFF scheme are further illustrated in the bar plots of Figure 4. Under BUB-0.3, stronger oxygen uptake occurs from spring to early summer (September–December). Except for the SIZ, all regions experience enhanced oxygen release from late summer to autumn (February–May), accompanied by a slight reduction in wintertime uptake. Relative to DIFF, the peak enhancement in oxygen uptake occurs in October for the STZ and SAZ, and in December for the PAZ and SIZ. The PAZ exhibits a maximum reduction of 6.7 ± 0.6 mmol m^{-2} d^{-1} in December. In contrast, the SIZ shows only a minor reduction in uptake during late winter, with enhanced uptake persisting throughout most of the year. Under the BUB-1.0 scheme, oxygen uptake is enhanced throughout the entire uptake season and oxygen release is intensified during the release season across all regions. For most regions, the maximum additional uptake occurs in winter. In the SIZ, where oxygen uptake dominates year-round, the BUB-1.0 scheme further amplifies this persistent uptake. These contrasting seasonal responses are associated with the nonlinear wind dependence of bubble injection and the seasonal evolution of surface O_2 disequilibrium, as discussed in Section 4.1.

Finally, to assess the robustness of these results, we examine the interannual variability of the integrated Southern Ocean air-sea O_2 flux (south of 30°S) over 2000–2014 under all three gas-exchange schemes (Figure S4 in

21699291, 2026, 9, Downloaded from https://agupubs.onlinelibrary.wiley.com/doi/10.1029/2026JC024425 by Jianping Huang - Lanzhou University , Wiley Online Library on [12/11/2026]. See the Terms and Conditions (https://onlinelibrary.wiley.com/terms-and-conditions) on Wiley Online Library for rules of use; OA articles are governed by the applicable Creative Commons License

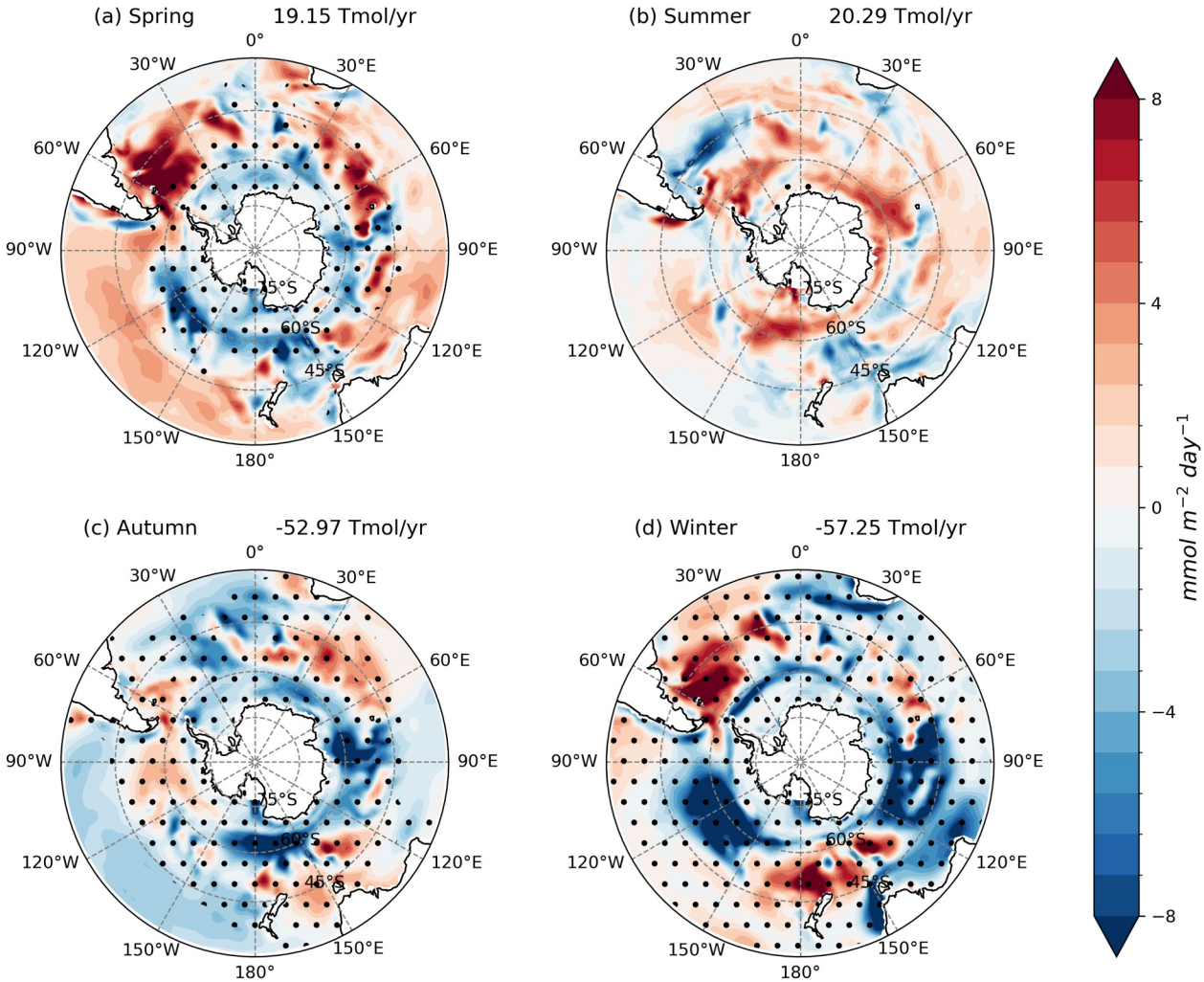


Figure 6. As in Figure 5, but for the seasonal-mean air-sea O_2 flux differences between BUB-1.0 and DIFF. Stippling denotes regions where the seasonal-mean DIFF flux is negative, indicating net oceanic O_2 uptake.

Supporting Information S1). The annual-mean flux fluctuates between approximately −100 and −130 Tmol yr^{-1}, and in most years the two bubble-mediated schemes exhibit more negative fluxes than the DIFF scheme, indicating systematically stronger O_2 uptake; only 2003, 2006, and 2007 show small reversals of this pattern. This persistent offset suggests that the enhanced uptake associated with bubble-mediated exchange is not driven by a few extreme years. In addition, we performed a sensitivity experiment in which the bubble-mediated gas-flux parameterization is activated from 1960 instead of 1940. The resulting Southern Ocean O_2 fluxes and spatial patterns are very similar to those of the main bubble runs (Figure S5 in Supporting Information S1), indicating that our conclusions are robust to the exact onset year of the bubble parameterization.

3.2. Assessment of the Parameterizations

Due to the limited spatial and temporal coverage of direct air-sea oxygen flux observations, we evaluate model performance indirectly using surface $\Delta[O_2]$, which serves as a more physically meaningful metric for model-observation comparison than raw dissolved O_2 (Section 2.5). Since dissolved oxygen is strongly influenced by local temperature and Argo profiles cannot be perfectly co-located with model output, $\Delta[O_2]$ provides a more robust metric for evaluation than raw concentrations. To ensure a consistent comparison with BGC-Argo data, we evaluate the model configurations specifically for the 2004–2014 period, matching the availability of the float observations. We then average both the observed and modeled $\Delta[O_2]$ over the four Southern Ocean regions and compare their seasonal cycles.

21699291, 2026, 9, Downloaded from https://agupubs.onlinelibrary.wiley.com/doi/10.1029/2026JC024425 by Jianping Huang - Lanzhou University , Wiley Online Library on [12/11/2026]. See the Terms and Conditions (https://onlinelibrary.wiley.com/terms-and-conditions) on Wiley Online Library for rules of use; OA articles are governed by the applicable Creative Commons License

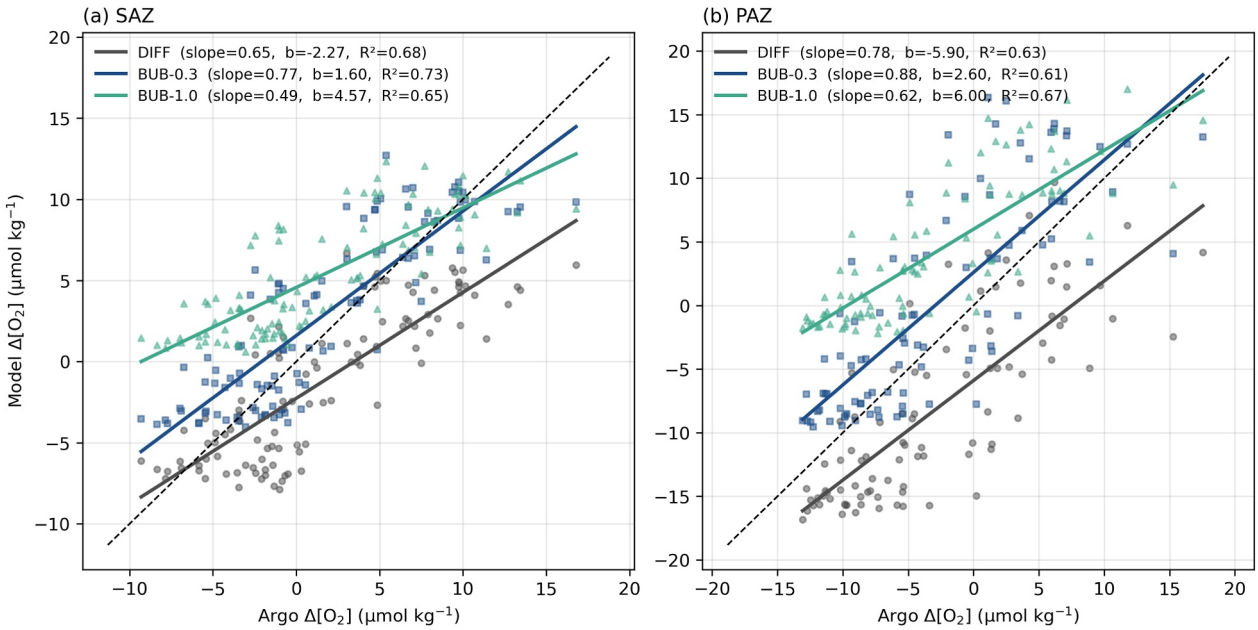


Figure 7. Comparison between monthly surface $\Delta[O_2]$ from Argo BGC float observations and regionally averaged model $\Delta[O_2]$ in the Subantarctic Zone (SAZ; a) and Polar Frontal-Antarctic Zone (PAZ; b) over 2004–2014. Each marker corresponds to a monthly mean. The dashed line denotes the 1:1 relationship. Solid lines show ordinary-least-squares regression fits for the three gas-exchange schemes (DIFF, BUB-0.3, and BUB-1.0), and the slope, intercept (b), and coefficient of determination (R^2) are given in the legend. Months with fewer than 10 Argo profiles within a region were excluded from the observational monthly means to avoid biases due to sparse sampling.

Figure 7 compares the monthly surface $\Delta[O_2]$ from Argo BGC float observations with the corresponding regionally averaged model $\Delta[O_2]$ in the SAZ and PAZ. Each point represents a monthly mean over 2004–2014, and the dashed line denotes the 1:1 reference line. Solid lines show ordinary least-squares fits for the three gas-exchange configurations (DIFF, BUB-0.3, and BUB-1.0), and the regression slope, intercept, and coefficient of determination (R^2) are given in the legend. In both regions, the diffusion-only scheme substantially underestimates $\Delta[O_2]$, as reflected by regression slopes well below unity and large negative intercepts (e.g., -2.3 μmol kg^{-1} in the SAZ and -5.9 μmol kg^{-1} in the PAZ). This bias indicates that the model response is too weak and systematically offset toward lower $\Delta[O_2]$ values. Incorporating bubble-mediated exchange increases the $\Delta[O_2]$ variability and shifts the regression lines toward the 1:1 line. The weak-bubble configuration (BUB-0.3) yields the highest correlations with observations ($R^2 \approx 0.73$ in the SAZ and 0.61 in the PAZ), with regression slopes (0.77–0.88) closest to unity and relatively small intercept biases. In contrast, the strong-bubble scheme (BUB-1.0) tends to over-amplify $\Delta[O_2]$, producing regression lines with shallower slopes (0.49–0.62) but large positive intercepts. These results demonstrate that including bubble-mediated air-sea exchange substantially improves the agreement between modeled and observed $\Delta[O_2]$, with the scaled bubble scheme (BUB-0.3) providing the most realistic $\Delta[O_2]$ variability and mean state across Southern Ocean regions.

The quantitative evaluation summarized in Table 1 shows that the effects of bubble-mediated exchange vary among Southern Ocean regions and depend on bubble strength. In the SAZ, BUB-0.3 provides the clearest improvement, producing the largest reduction in RMSE and a substantial decrease in absolute bias, whereas BUB-1.0 tends to overshoot and introduces a positive bias. In the STZ, the improvements are more limited: BUB-1.0 reduces the mean bias but slightly degrades the correlation. In the PAZ and SIZ, the bubble-mediated configurations partially reduce the negative model bias, although the observed variability remains difficult to reproduce, likely because of uncertainties associated with deep mixing and sea-ice-related processes. Overall, BUB-0.3 provides the best balance among bias, RMSE, and correlation across the evaluated regions, although the magnitude of improvement is not spatially uniform. The complete regional seasonal cycles are provided in Figure S6 in Supporting Information S1 as additional diagnostic information.

To further assess whether the influence of bubble-mediated exchange extends beyond the immediate surface and is retained within newly ventilated waters, we evaluated O_2 concentrations in PSAMW using collocated

21699291, 2026, 9, Downloaded from https://agupubs.onlinelibrary.wiley.com/doi/10.1029/2026JC024425 by Jianping Huang - Lanzhou University , Wiley Online Library on [12/11/2026]. See the Terms and Conditions (https://onlinelibrary.wiley.com/terms-and-conditions) on Wiley Online Library for rules of use; OA articles are governed by the applicable Creative Commons License

21699291, 2026, 9, Downloaded from https://agupubs.onlinelibrary.wiley.com/doi/10.1029/2026JC024425 by Jianping Huang - Lanzhou University , Wiley Online Library on [12/11/2026]. See the Terms and Conditions (https://onlinelibrary.wiley.com/terms-and-conditions) on Wiley Online Library for rules of use; OA articles are governed by the applicable Creative Commons License

Table 1
Statistical Comparison of Simulated Surface $\Delta[O_2]$ Against Biogeochemical Argo Float Observations Across Four Southern Ocean Regions

Region	Model	Bias (μmol kg^{-1})	RMSE (μmol kg^{-1})
STZ	DIFF	−2.5	2.71
	BUB-0.3	−3	3.14
	BUB-1.0	−1.81	2.46
SAZ	DIFF	−2.8	3.5
	BUB-0.3	1.24	2.3
	BUB-1.0	3.79	4.56
PAZ	DIFF	−4.8	5.62
	BUB-0.3	3.52	4.96
	BUB-1.0	7.56	7.97
SIZ	DIFF	−6.97	10.46
	BUB-0.3	1.66	8.99
	BUB-1.0	9.3	11.6

Note. The metrics include mean Bias and Root-Mean-Square Error (RMSE) for the diffusion-only scheme (DIFF) and two bubble-mediated schemes (BUB-0.3 and BUB-1.0).

BGC-Argo+ profiles and model fields (Figure 8). PSAMW forms within deep winter mixed layers and is subsequently subducted into the ocean interior, thereby providing an integrated constraint on whether the influence of surface bubble-mediated exchange is retained in newly ventilated waters. Its inclusion in recent wind-wave-bubble studies also enables a relatively direct comparison across parameterizations and model configurations. The DIFF simulation generally produces lower dissolved O_2 concentrations than observed over much of the sampled potential-temperature range, indicating excessive oxygen undersaturation during PSAMW formation. BUB-0.3 shifts the modeled potential temperature-O_2 relationship toward the observations while retaining the observed tendency toward modest undersaturation. In contrast, BUB-1.0 produces systematically higher O_2 concentrations, with the saturation-anomaly distribution concentrated near or slightly above atmospheric equilibrium.

We quantified the agreement between the modeled and observed saturation-anomaly distributions using the Earth Mover's Distance (D). BUB-0.3 reduces the model-observation distance by 73.2% relative to DIFF, whereas

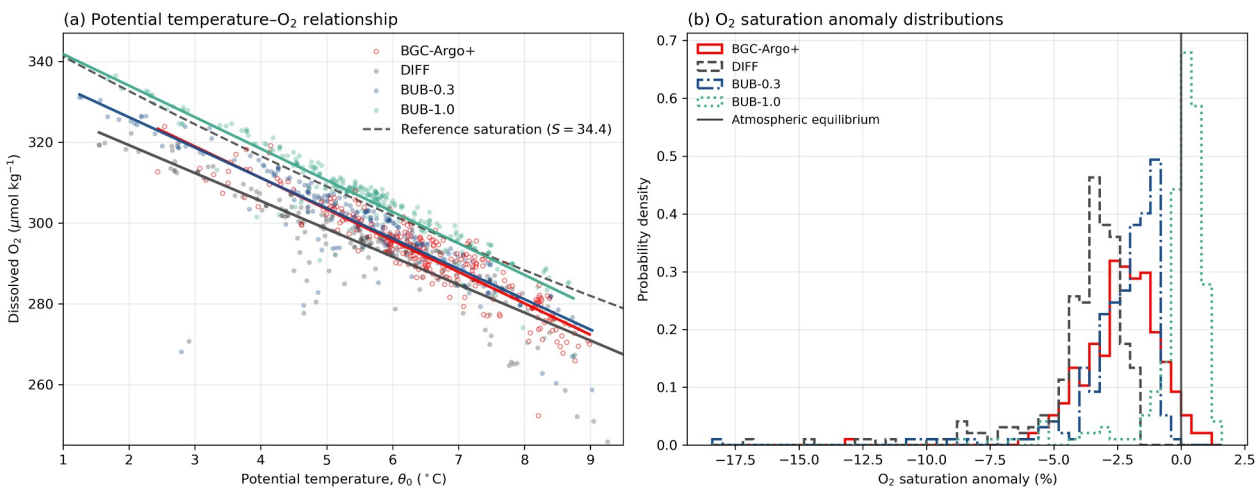


Figure 8. Evaluation of simulated oxygen in Pacific Subantarctic Mode Water (PSAMW). (a) Relationship between potential temperature and dissolved O_2 for collocated BGC-Argo+ observations and the DIFF, BUB-0.3, and BUB-1.0 simulations. The dashed curve denotes atmospheric equilibrium calculated at a representative salinity of 34.4 and is shown for visual reference only. Solid lines show ordinary least-squares regressions for the observations and three model configurations. (b) Probability density distributions of O_2 saturation anomaly, calculated using the temperature and salinity of each sample. The vertical dashed line indicates atmospheric equilibrium.

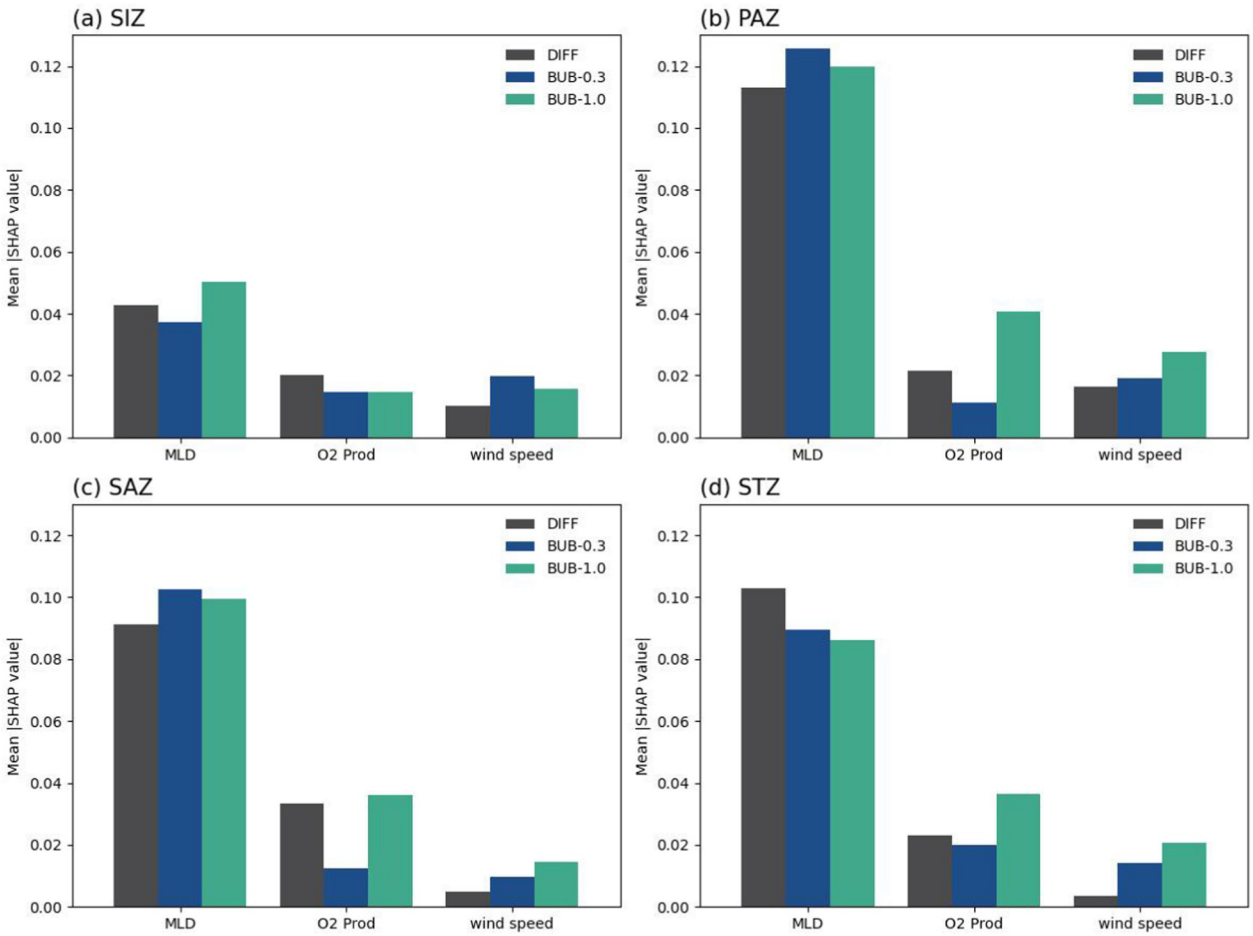


Figure 9. Relative importance of mixed-layer depth (MLD), mixed-layer integrated gross oxygen production, and 10-m wind speed in explaining non-thermal air-sea O_2 flux anomalies, as quantified by SHAP values from the LightGBM model. Each panel corresponds to one Southern Ocean region (STZ, SAZ, PAZ, SIZ), and colors denote different gas-exchange parameterizations (DIFF, BUB-0.3, BUB-1.0). Bars show mean absolute SHAP values averaged over all samples in that region, providing a normalized measure of the contribution of each predictor to the variance of non-thermal air-sea O_2 flux.

BUB-1.0 increases the model-observation mismatch by 40.8% relative to DIFF. Thus, moderate bubble injection improves both the position and shape of the modeled PSAMW saturation distribution, whereas the unscaled bubble formulation overcorrects the undersaturation bias.

3.3. Process Attribution of Air-Sea O_2 Flux Variability

Consistent with established Southern Ocean seasonality, $F_{nonthermal}$ generally becomes more negative with increasing mixed-layer depth and wind speed and more positive with increasing O_2 production across the four regions (Figures S7-S9 in Supporting Information S1). The relationships also exhibit spring-autumn hysteresis, reflecting the seasonal phasing of biological production, vertical mixing, and surface $\Delta[O_2]$. To quantify the relative importance of these competing processes across different bubble parameterization schemes, we next use the LightGBM-SHAP framework described in Section 2.6 to examine how the relative contributions of these predictors vary among regions and gas-exchange configurations. Figure 9 summarizes the global SHAP feature importance and reveals a regime shift in the physical control of gas exchange. In the open-ocean regions (STZ, SAZ, and PAZ), the importance of wind speed increases monotonically with bubble injection intensity. The SHAP summary plots (Figure S10 in Supporting Information S1) further demonstrate a qualitative change in mechanism: in the diffusion-only scheme, the wind effect is relatively symmetric and constrained, consistent with wind speed acting primarily through the transfer velocity, whereas bubble-enabled schemes produce a highly asymmetric, nonlinear response with a long tail of large positive SHAP values at high winds, indicating that wind events become an active source of oxygen injection.

21699291, 2026, 9, Downloaded from https://agupubs.onlinelibrary.wiley.com/doi/10.1029/2026JC024425 by Jianping Huang - Lanzhou University , Wiley Online Library on [12/11/2026]. See the Terms and Conditions (https://onlinelibrary.wiley.com/terms-and-conditions) on Wiley Online Library for rules of use; OA articles are governed by the applicable Creative Commons License

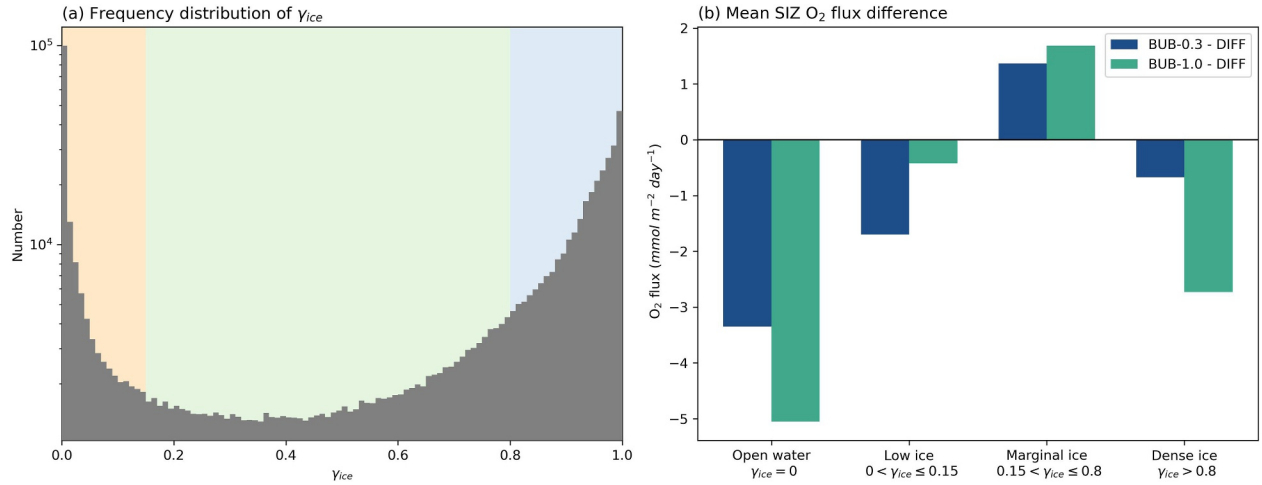


Figure 10. Sea-ice concentration distribution and its relationship with bubble-induced changes in air-sea O_2 flux in the seasonal ice zone. (a) Frequency distribution of sea-ice concentration, γ_{ice}, shown on a logarithmic scale. The shaded regions denote open water ($\gamma_{ice} = 0$), low-ice conditions ($0 < \gamma_{ice} \leq 0.15$), marginal-ice conditions ($0.15 < \gamma_{ice} \leq 0.8$), and dense-ice conditions ($\gamma_{ice} > 0.8$). (b) Mean differences in air-sea O_2 flux between the BUB-0.3 and DIFF simulations and between the BUB-1.0 and DIFF simulations for the four sea-ice categories. Positive and negative values indicate higher and lower O_2 fluxes, respectively, relative to the DIFF simulation.

Despite the increasing role of wind speed in bubble-injecting schemes, the SHAP analysis establishes a clear global hierarchy of drivers. MLD remains the dominant first-order driver across all parameterizations, consistently exhibiting the highest feature importance. This confirms that the seasonal cycle of stratification and deep convection sets the fundamental potential for air-sea exchange by determining the background saturation state. Intriguingly, while MLD governs the baseline, the biological response exhibits a complex, non-linear sensitivity to parameterization, displaying a "U-shaped" pattern of importance. We propose that the moderate bubble injection in the BUB-0.3 scheme introduces noise that masks biological signals, whereas the strong injection in the BUB-1.0 scheme maintains a background state of near-saturation. In this "filled cup" scenario, the mixed layer has reduced buffering capacity against oxygen addition; consequently, any new biological oxygen production is efficiently vented to the atmosphere, thereby enhancing the model's sensitivity to biological variability.

To examine how the response to the bubble-inclusive formulations varies with sea-ice conditions, we classified the SIZ grid-cell samples into four sea-ice concentration regimes (Figure 10a) and calculated the corresponding mean BUB-DIFF flux differences (Figure 10b). Here, flux anomalies are defined as $F_{\mathrm{BUB}} - F_{\mathrm{DIFF}}$, with negative values indicating enhanced oceanic O_2 uptake.

The largest enhancement of oceanic O_2 uptake occurs under open-water conditions, with mean flux differences of -3.35 and -5.05 mmol m^{-2} d^{-1} for BUB-0.3 and BUB-1.0, respectively. Under low-ice conditions, the differences remain negative but decrease in magnitude. In contrast, marginal-ice conditions are associated with positive differences of 1.37–1.69 mmol m^{-2} d^{-1}, indicating reduced uptake or enhanced outgassing relative to DIFF. Negative differences re-emerge under dense-ice conditions, reaching -0.67 and -2.73 mmol m^{-2} d^{-1} for BUB-0.3 and BUB-1.0, respectively. The resulting nonmonotonic variation indicates that the BUB-DIFF response is not determined by sea-ice concentration alone, but also reflects covarying seasonal changes in wind forcing, surface O_2 disequilibrium, and upper-ocean mixing.

4. Discussion

4.1. Seasonal and Regional Dependence of Bubble-Mediated O_2 Exchange

In the SAZ, the annual-mean O_2 flux remains close to zero under all three gas-exchange configurations. This near-zero annual mean does not reflect uniformly weak air-sea exchange or small $\Delta[O_2]$ throughout the year. Instead, it results primarily from seasonal compensation between pronounced austral-summer outgassing and wintertime uptake (Figure 4b). The BUB–DIFF flux anomalies also reverse sign over the seasonal cycle, such that opposing monthly responses largely cancel when integrated over the year. Consequently, the relatively small annual-mean differences among the configurations mask substantial seasonal responses.

21699291, 2026, 9, Downloaded from https://agupubs.onlinelibrary.wiley.com/doi/10.1029/2026JC024425 by Jianping Huang - Lanzhou University , Wiley Online Library on [12/11/2026]. See the Terms and Conditions (https://onlinelibrary.wiley.com/terms-and-conditions) on Wiley Online Library for rules of use; OA articles are governed by the applicable Creative Commons License

21699291, 2026, 9, Downloaded from https://agupubs.onlinelibrary.wiley.com/doi/10.1029/2026JC024425 by Jianping Huang - Lanzhou University , Wiley Online Library on [12/11/2026]. See the Terms and Conditions (https://onlinelibrary.wiley.com/terms-and-conditions) on Wiley Online Library for rules of use; OA articles are governed by the applicable Creative Commons License

More broadly, the contrasting seasonal responses of the BUB-0.3 and BUB-1.0 reflect the nonlinear dependence of bubble-mediated gas exchange on wind speed and its interaction with the seasonal evolution of surface $\Delta[O_2]$. In Liang et al. (2013)'s parameterization, small-bubble injection dominates gas exchange under high wind conditions. During autumn and winter, Southern Ocean wind speeds intensify, leading to vigorous small-bubble injection in the BUB-1.0 scheme. Even when subsurface waters are strongly undersaturated, the enhanced bubble injection efficiently compensates for the O_2 deficit. As shown by the $\Delta[O_2]$ distributions (Figure S3 in Supporting Information S1), under extreme wind events this process can rapidly drive surface waters toward saturation or even transient supersaturation. Consequently, BUB-1.0 substantially increases oxygen uptake during autumn and winter. The excess oxygen absorbed during autumn and winter causes surface waters to reach thermodynamic equilibrium earlier in the seasonal cycle. As a result, during spring and summer the air-sea O_2 gradient weakens or reverses, leading to reduced uptake or enhanced oxygen release relative to the diffusion-only scheme. In contrast to the BUB-1.0 scheme, the magnitude of wintertime O_2 uptake under BUB-0.3 is substantially weaker due to the downscaled bubble term, such that air-sea gas exchange over the Southern Ocean can be weaker under BUB-0.3 than under the DIFF scheme. In this configuration, small-bubble injection becomes dominant only under more extreme wind speeds. During spring, the combination of rapidly evolving surface $\Delta[O_2]$ and persistently elevated wind speeds allows bubble-mediated processes to substantially enhance oxygen uptake, leading to a pronounced springtime enhancement under the BUB-0.3 scheme.

4.2. Sources of Model-Observation Discrepancies in the PAZ and SIZ

The PAZ is a major region of Southern Ocean O_2 uptake and exhibits the largest seasonal amplitude in air-sea O_2 flux among the four regions. Near-surface $\Delta[O_2]$ in this region is strongly influenced by high winds, seasonal mixed-layer deepening, entrainment of O_2-poor subsurface waters, and subsequent spring restratification. Consequently, biases in the timing or magnitude of mixed-layer evolution and entrainment can produce substantial errors in simulated $\Delta[O_2]$, even when the broad seasonal cycle is reproduced. Potential deficiencies include an overly deep or shallow winter mixed layer, biases in the timing of seasonal convection and restratification, and inaccuracies in the O_2 concentration of waters entrained into the mixed layer. An additional source of mismatch is that the CESM2 experiments are freely evolving coupled historical simulations rather than ocean hindcast simulations driven by observed atmospheric variability. The simulated atmosphere and ocean are constrained by historical external forcings, but internally generated storms and interannual variability are not synchronized with the exact timing and location of BGC-Argo observations, which is particularly important in the dynamically active PAZ. Therefore, the relatively large PAZ bias and RMSE likely reflect a combination of uncertainties in vertical mixing, entrainment, subsurface O_2 distributions, internal climate variability, and observational sampling, rather than a deficiency in any single process.

In the SIZ, uncertainties in both sea-ice and upper-ocean processes may contribute to the remaining discrepancies. As discussed in Section 3.3, sea ice directly suppresses gas exchange by reducing the open-water area available for wind-wave breaking and bubble entrainment. However, marginal-ice conditions typically occur during seasonal ice advance or retreat, when upper-ocean stratification, mixed-layer depth, biological production, wind forcing, and surface $\Delta[O_2]$ are also changing rapidly. The positive anomalies under marginal-ice conditions may therefore reflect the combined effects of these covarying processes rather than a direct response to intermediate sea-ice concentration. In particular, bubble-mediated gas exchange may drive surface waters closer to O_2 saturation, thereby reducing the air-sea concentration gradient available for further oceanic uptake and, under some conditions, producing greater outgassing relative to the diffusion-only simulation.

Although dense sea ice strongly suppresses gas exchange, residual bubble-related flux anomalies may persist over the open-water fraction of partially ice-covered grid cells. The magnitude of the residual anomaly may also reflect the concurrent effects of wind forcing, mixed-layer conditions, and $\Delta[O_2]$ and should not be attributed to sea-ice concentration alone. CESM2 accounts for the first-order effect of sea ice by scaling gas fluxes with the open-water fraction, but it does not explicitly resolve leads and polynyas, wave-ice interactions, ice-edge wave breaking, or gas transport through and beneath sea ice. These unresolved processes, together with biases in sea-ice seasonality and upper-ocean mixing, may contribute to the remaining model-observation discrepancies in the SIZ.

Observational representativeness provides an additional limitation in both regions. BGC-Argo coverage is spatially and seasonally uneven, particularly in ice-covered waters, and the simulated monthly regional means are not perfectly colocated with individual float observations. Furthermore, near-surface $\Delta[O_2]$ primarily evaluates

21699291, 2026, 9, Downloaded from https://agupubs.onlinelibrary.wiley.com/doi/10.1029/2026JC024425 by Jianping Huang - Lanzhou University , Wiley Online Library on [12/11/2026]. See the Terms and Conditions (https://onlinelibrary.wiley.com/terms-and-conditions) on Wiley Online Library for rules of use; OA articles are governed by the applicable Creative Commons License

the immediate air-sea boundary condition and does not fully constrain the vertical redistribution or long-term storage of oxygen. The remaining PAZ and SIZ discrepancies should therefore be interpreted as the combined outcome of gas-exchange parameterization, vertical mixing and entrainment, regional sea-ice and ocean dynamics, internal climate variability, and observational sampling.

4.3. Water-Mass Constraints on Bubble Strength and Comparison With Recent Studies

The PSAMW evaluation provides a direct basis for assessing how the Liang et al. (2013) formulation compares with the recent wind-wave-bubble framework of Deike et al. (2025) and Rustogi et al. (2026). Although both approaches represent bubble-driven asymmetric gas exchange, their formulations are not directly equivalent. Liang et al. separate bubble fluxes according to bubble size and dissolution behavior into partially dissolving large bubbles and fully dissolving small bubbles, whereas Deike et al. (2025) decompose bubble-mediated exchange into symmetric and asymmetric components and explicitly account for wave state and gas-solubility effects. Therefore, the tuning factor β in the Liang scheme, which scales both bubble components simultaneously, cannot be directly mapped onto the independently calibrated symmetric and asymmetric coefficients in the Deike formulation. Moreover, because the bubble terms in the Liang formulation increase more steeply with wind forcing, the unscaled BUB-1.0 configuration can produce excessively strong bubble injection under the high-wind conditions of the Southern Ocean.

Despite these structural differences, the improvement obtained with BUB-0.3 is broadly consistent with recent wind-wave-bubble simulations. In PSAMW, BUB-0.3 reduces the Earth Mover's Distance between the simulated and BGC-Argo+ oxygen-saturation distributions by 73.2% relative to DIFF. This improvement is comparable to Rustogi et al. (2026)'s work. Together with the improved representation of surface $\Delta[O_2]$, the PSAMW results provide complementary evidence that asymmetric bubble exchange is important for reproducing both near-surface $\Delta[O_2]$ and the oxygen content of newly ventilated waters.

Importantly, our sensitivity experiments show that stronger bubble injection does not lead to a monotonic improvement in model performance. BUB-1.0 shifts the simulated PSAMW distribution toward atmospheric equilibrium and slight supersaturation, increasing the model-observation distance by 40.8% relative to DIFF. This deterioration suggests that the unscaled Liang formulation produces excessively strong effective bubble injection in PSAMW under the high-wind conditions simulated by CESM2. Nevertheless, the superior performance of BUB-0.3 should not be interpreted as evidence for a universally optimal bubble coefficient. PSAMW oxygen concentrations are jointly controlled by air-sea exchange, mixed-layer deepening, entrainment, circulation, and water-mass formation, and a reduced bubble coefficient may partly compensate for CESM2-specific biases in vertical mixing or ventilation.

Despite these limitations, the present study extends recent ocean-only investigations by evaluating bubble-mediated exchange online within a fully coupled Earth system model, in which atmospheric winds, ocean circulation and mixing, and sea-ice conditions evolve within a dynamically consistent climate framework. The agreement between the PSAMW improvement obtained with BUB-0.3 and that reported using the Deike formulation suggests that the need to represent asymmetric bubble exchange is robust across different parameterizations and model configurations. At the same time, the contrasting performance of BUB-0.3 and BUB-1.0 demonstrates that explicitly including bubbles is not sufficient by itself; the magnitude and environmental dependence of bubble-mediated transfer must also be constrained against observations. Thus, our results identify BUB-0.3 as the better-performing configuration among those tested in CESM2, rather than as a universally optimal scaling, and motivate future implementation of explicitly wave-dependent formulations in fully coupled Earth system models.

4.4. Implications for Southern Ocean O_2 Change and Interior Ventilation

Previous studies have identified the Southern Ocean as a hotspot of climate-driven O_2 change. Matear et al. (2000) projected particularly large changes in Southern Ocean air-sea O_2 exchange under climate warming, primarily because enhanced stratification weakens convective ventilation and the subduction of oxygenated surface waters. Observation-based analyses have likewise revealed substantial but spatially heterogeneous changes in the global ocean O_2 inventory over recent decades (Schmidtko et al., 2017). Our experiments do not directly quantify long-term deoxygenation trends, because they focus on the historical mean state and its sensitivity to the choice of air-sea gas-exchange formulation. Nevertheless, the results demonstrate that this choice materially affects the

simulated surface O_2 boundary condition. Relative to DIFF, the bubble-inclusive configurations increase the 2000–2014 mean Southern Ocean O_2 uptake by approximately 13%–19%, with the largest responses occurring in high-wind and high-latitude regions.

These results indicate that simulations of Southern Ocean O_2 change may depend not only on solubility, stratification, and overturning circulation, but also on the interaction of gas-exchange parameterization with wind forcing, surface $\Delta[O_2]$, mixed-layer evolution, and sea-ice cover. Changes in bubble-mediated exchange could therefore modify the surface supply of O_2 under future climate conditions. However, neither the sign nor the magnitude of this effect can be inferred directly from the present historical-mean experiments, because future changes in winds, wave conditions, sea ice, stratification, and surface $\Delta[O_2]$ may exert competing influences. Addressing this question will require transient climate-change simulations using consistently implemented gas-exchange formulations.

The observational comparisons provide constraints at two related but distinct levels. The regional BGC-Argo comparison primarily evaluates near-surface $\Delta[O_2]$ relevant to air-sea exchange, whereas the PSAMW analysis provides an initial constraint on whether differences generated near the surface are retained in newly ventilated mode waters. The improved PSAMW agreement under BUB-0.3 suggests that the influence of the gas-exchange formulation is not necessarily confined to the immediate surface layer. Nevertheless, these comparisons do not constitute a validation of the complete ocean O_2 inventory. The penetration and persistence of additional oxygen below the mixed layer depend on entrainment, subduction, lateral transport, biological consumption, and water-mass circulation. Improved agreement in near-surface $\Delta[O_2]$ or PSAMW oxygen properties therefore does not necessarily imply an equally accurate representation of subsurface O_2 concentrations, whole-column storage, or long-term deoxygenation. A comprehensive assessment would require depth-resolved water-mass comparisons and explicit analysis of changes in the interior O_2 inventory.

5. Conclusions

This study implemented the bubble-mediated air-sea gas-exchange formulation of Liang et al. (2013) in the fully coupled CESM2 Earth system model and evaluated its influence on Southern Ocean O_2 exchange. Replacing the diffusion-only formulation with the bubble-mediated configurations increased the magnitude of the 2000–2014 mean Southern Ocean O_2 uptake from 96.6 Tmol yr^{-1} under DIFF to 108.7 and 114.5 Tmol yr^{-1} under BUB-0.3 and BUB-1.0, corresponding to increases of approximately 12.5% and 18.5%, respectively. The response was spatially and seasonally heterogeneous. Bubble-inclusive exchange generally strengthened O_2 uptake in the high-latitude PAZ and SIZ, while seasonal reversals in the BUB-DIFF flux differences produced substantial compensation in the SAZ. Within the SIZ, the flux response varied nonmonotonically across sea-ice regimes, reflecting the combined effects of open-water availability and covarying changes in wind forcing, surface $\Delta[O_2]$, and upper-ocean mixing.

Comparison with collocated BGC-Argo+ observations shows that the influence of bubble strength is not monotonic. BUB-0.3 reduced the near-surface $\Delta[O_2]$ RMSE in three of the four Southern Ocean regions, including an approximately 34% reduction in the SAZ, whereas BUB-1.0 frequently shifted surface waters too close to or above atmospheric equilibrium. Consistent behavior was found in PSAMW: BUB-0.3 reduced the Earth Mover's Distance between the modeled and observed O_2-saturation-anomaly distributions by 73.2% relative to DIFF, whereas BUB-1.0 increased the mismatch by 40.8%. These results identify BUB-0.3 as the better-performing configuration among those tested in CESM2, while also indicating that an optimal bubble strength is likely to depend on regional conditions and may partly compensate for model-specific biases in mixing, ventilation, or water-mass formation.

The process-attribution analysis further indicates that mixed-layer depth remains the leading predictor of nonthermal air-sea O_2 flux variability across all configurations, while the relative importance and nonlinear influence of wind speed increase under the bubble-inclusive formulations. These relationships support a physical interpretation in which upper-ocean mixing establishes the background $\Delta[O_2]$ available for exchange, whereas strong winds increasingly affect the magnitude of inward O_2 transfer when bubble pathways are represented. However, the statistical attribution does not by itself establish causal contributions, and the interactions among wind forcing, biology, mixed-layer evolution, and surface $\Delta[O_2]$ require further process-based evaluation.

21699291, 2026, 9, Downloaded from https://agupubs.onlinelibrary.wiley.com/doi/10.1029/2026JC024425 by Jianping Huang - Lanzhou University , Wiley Online Library on [12/11/2026]. See the Terms and Conditions (https://onlinelibrary.wiley.com/terms-and-conditions) on Wiley Online Library for rules of use; OA articles are governed by the applicable Creative Commons License

Overall, the results demonstrate that the choice and calibration of air-sea gas-exchange formulation materially affect simulated Southern Ocean O_2 uptake, its seasonal cycle, and the oxygen properties of newly ventilated waters. Improved agreement in near-surface $\Delta[O_2]$ and PSAMW does not, however, constitute a validation of the complete ocean O_2 inventory or its long-term trend. Future work should evaluate bubble-inclusive formulations in transient climate-change and ensemble simulations, implement explicitly wave-dependent exchange schemes in coupled Earth system models, and use depth-resolved observations and multiple dissolved gases to constrain both surface exchange and the subsequent transport and storage of oxygen in the ocean interior.

Conflict of Interest

The authors declare no conflicts of interest relevant to this study.

Availability Statement

The analysis scripts and processed data supporting this study are archived on Zenodo (Wang et al., 2026; https://doi.org/10.5281/zenodo.19042651).

Acknowledgments
The bubble-mediated gas transfer parameterization in this study is implemented based on the open-source Gas Exchange Toolbox (https://github.com/dnicholson/gas_toolbox). This work was jointly supported by the National Science Foundation of China (Grants 42406196, 42488201), the Natural Science Foundation of Gansu Province, China (Grant 26JRRA240), the Lanzhou Special Fund for Talent Program, the China 111 project (Grant B13045), the Fundamental Research Funds for the Central Universities (Grant lzujbky-2024-pd06) and the Postdoctoral Fellowship Program of CPSF (Grant GZC20231000). The simulations and data analysis are supported by Supercomputing Center of Lanzhou University. The authors thank Dr. Yuanxu Dong of the GEOMAR Helmholtz Centre for Ocean Research Kiel for his helpful suggestions.

References

Atamanchuk, D., Koelling, J., Send, U., & Wallace, D. W. R. (2020). Rapid transfer of oxygen to the deep ocean mediated by bubbles. *Nature Geoscience*, *13*(3), 232–237. https://doi.org/10.1038/s41561-020-0532-2

Bopp, L., Resplandy, L., Orr, J. C., Doney, S. C., Dunne, J. P., Gehlen, M., et al. (2013). Multiple stressors of ocean ecosystems in the 21st century: Projections with CMIP5 models. *Biogeosciences*, *10*(10), 6225–6245. https://doi.org/10.5194/bg-10-6225-2013

Breitburg, D., Levin, L. A., Oschlies, A., Grégoire, M., Chavez, F. P., Conley, D. J., et al. (2018). Declining oxygen in the global ocean and coastal waters. *Science*, *359*(6371), eaam7240. https://doi.org/10.1126/science.aam7240

Bushinsky, S. M. (2025). BGC Argo Plus Code Repository [Software]. *GitHub*. Retrieved from https://github.com/Hi-Cycles/BGC_Argo_Plus_Code_Repository

Bushinsky, S. M., & Emerson, S. (2015). Marine biological production from in situ oxygen measurements on a profiling float in the subarctic Pacific Ocean. *Global Biogeochemical Cycles*, *29*(12), 2050–2060. https://doi.org/10.1002/2015GB005251

Bushinsky, S. M., Gray, A. R., Johnson, K. S., & Sarmiento, J. L. (2017). Oxygen in the Southern Ocean from argo floats: Determination of processes driving air-sea fluxes. *Journal of Geophysical Research: Oceans*, *122*(11), 8661–8682. https://doi.org/10.1002/2017JC012923

Bushinsky, S. M., Nachod, Z., Fassbender, A. J., Tamsitt, V., Takeshita, Y., & Williams, N. (2025). Offset between profiling float and shipboard oxygen observations at depth imparts bias on float pH and derived $p\,CO_2$. *Global Biogeochemical Cycles*, *39*(5), e2024GB008185. https://doi.org/10.1029/2024GB008185

Chen, X., & Tung, K.-K. (2014). Varying planetary heat sink led to global-warming slowdown and acceleration. *Science*, *345*(6199), 897–903. https://doi.org/10.1126/science.1254937

Cheng, L., Trenberth, K. E., Fasullo, J., Boyer, T., Abraham, J., & Zhu, J. (2017). Improved estimates of ocean heat content from 1960 to 2015. *Science Advances*, *3*(3), e1601545. https://doi.org/10.1126/sciadv.1601545

Danabasoglu, G., Bates, S. C., Briegleb, B. P., Jayne, S. R., Jochum, M., Large, W. G., et al. (2012). The CCSM4 ocean component. *Journal of Climate*, *25*(5), 1361–1389. https://doi.org/10.1175/JCLI-D-11-00091.1

Danabasoglu, G., Lamarque, J. F., Bacmeister, J., Bailey, D. A., DuVivier, A. K., Edwards, J., et al. (2020). The community Earth system model version 2 (CESM2). *Journal of Advances in Modeling Earth Systems*, *12*(2), e2019MS001916. https://doi.org/10.1029/2019MS001916

Deike, L., Zhou, X., Rustogi, P., Stanley, R. H. R., Reichl, B. G., Bushinsky, S. M., & Resplandy, L. (2025). A universal wind–wave–bubble formulation for air–sea gas exchange and its impact on oxygen fluxes. *Proceedings of the National Academy of Sciences*, *122*(38), e2419319122. https://doi.org/10.1073/pnas.2419319122

Dong, Y., Bakker, D. C. E., Bell, T. G., Yang, M., Landschützer, P., Hauck, J., et al. (2024). Direct observational evidence of strong CO_2 uptake in the Southern Ocean. *Science Advances*, *10*(30), eadn5781. https://doi.org/10.1126/sciadv.adn5781

Dong, Y., Yang, M., Bell, T. G., Marandino, C. A., & Woolf, D. K. (2025). Asymmetric bubble-mediated gas transfer enhances global ocean CO_2 uptake. *Nature Communications*, *16*(1), 10595. https://doi.org/10.1038/s41467-025-66652-5

Du, J., Cheng, L., Ito, T., Garcia, H. E., Wang, Z., Sharp, J. D., et al. (2026). Climatology and annual cycle of global ocean dissolved oxygen represented by multiple observational gridded products. *Ocean Science*, *22*(3), 1483–1499. https://doi.org/10.5194/os-22-1483-2026

Eddebbar, Y. A., Long, M. C., Resplandy, L., Rödenbeck, C., Rodgers, K. B., Manizza, M., & Keeling, R. F. (2017). Impacts of ENSO on air-sea oxygen exchange: Observations and mechanisms. *Global Biogeochemical Cycles*, *31*(5), 901–921. https://doi.org/10.1002/2017GB005630

Emerson, S., & Bushinsky, S. (2016). The role of bubbles during air-sea gas exchange. *Journal of Geophysical Research: Oceans*, *121*(6), 4360–4376. https://doi.org/10.1002/2016JC011744

Emerson, S., Yang, B., White, M., & Cronin, M. (2019). Air-sea gas transfer: Determining bubble fluxes with in situ N_2 observations. *Journal of Geophysical Research: Oceans*, *124*(4), 2716–2727. https://doi.org/10.1029/2018JC014786

Eyring, V., Bony, S., Meehl, G. A., Senior, C. A., Stevens, B., Stouffer, R. J., & Taylor, K. E. (2016). Overview of the coupled model intercomparison project phase 6 (CMIP6) experimental design and organization. *Geoscientific Model Development*, *9*(5), 1937–1958. https://doi.org/10.5194/gmd-9-1937-2016

Frölicher, T. L., Rodgers, K. B., Stock, C. A., & Cheung, W. W. L. (2016). Sources of uncertainties in 21st century projections of potential ocean ecosystem stressors. *Global Biogeochemical Cycles*, *30*(8), 1224–1243. https://doi.org/10.1002/2015GB005338

Garcia, H. E., & Gordon, L. I. (1992). Oxygen solubility in seawater: Better fitting equations. *Limnology and Oceanography*, *37*(6), 1307–1312. https://doi.org/10.4319/LO.1992.37.6.1307

Huang, J., Liu, X., He, Y., Shen, S., Hou, Z., Li, S., et al. (2021). The oxygen cycle and a habitable Earth. Science China Earth sciences. *Science in China Press*, *64*(4), 511–528. https://doi.org/10.1007/s11430-020-9747-1

21699291, 2026, 9, Downloaded from https://agupubs.onlinelibrary.wiley.com/doi/10.1029/2026JC024425 by Jianping Huang - Lanzhou University , Wiley Online Library on [12/11/2026]. See the Terms and Conditions (https://onlinelibrary.wiley.com/terms-and-conditions) on Wiley Online Library for rules of use; OA articles are governed by the applicable Creative Commons License

Hurrell, J. W., Holland, M. M., Gent, P. R., Ghan, S., Kay, J. E., Kushner, P. J., et al. (2013). The community Earth system model: A framework for collaborative research. *Bulletin of the American Meteorological Society*, *94*(9), 1339–1360. https://doi.org/10.1175/BAMS-D-12-00121.1

Ito, T., Garcia, H. E., Wang, Z., Cheng, L., Du, J., Roach, C. J., et al. (2025). Assessing the observational uncertainties of dissolved oxygen climatology and seasonal cycle through a coordinated intercomparison project. *Global Biogeochemical Cycles*, *39*(11), e2025GB008751. https://doi.org/10.1029/2025GB008751

Ito, T., Garcia, H. E., Wang, Z., Minobe, S., Long, M. C., Cebrian, J., et al. (2024). Underestimation of multi-decadal global O_2 loss due to an optimal interpolation method. *Biogeosciences*, *21*(3), 747–759. https://doi.org/10.5194/bg-21-747-2024

Ke, G., Meng, Q., Finley, T., Wang, T., Chen, W., Ma, W., et al. (2017). LightGBM: A highly efficient gradient boosting decision tree. In I. Guyon, U. V. Luxburg, S. Bengio, H. Wallach, R. Fergus, S. Vishwanathan, et al. (Eds.), *Advances in neural information processing systems* (Vol. 30). Curran Associates, Inc. Retrieved from https://proceedings.neurips.cc/paper_files/paper/2017/file/6449f44a102fde848669bdd9eb6b76fa-Paper.pdf

Keeling, R. E., Körtzinger, A., & Gruber, N. (2010). Ocean deoxygenation in a warming world. *Annual Review of Marine Science*, *2*(1), 199–229. https://doi.org/10.1146/annurev.marine.010908.163855

Keeling, R. F., & Garcia, H. E. (2002). The change in Oceanic O_2 inventory associated with recent global warming. *Proceedings of the National Academy of Sciences of the United States of America*, *99*(12), 7848–7853. https://doi.org/10.1073/pnas.122154899

Keeling, R. F., Najjar, R. P., Bender, M. L., & Tans, P. P. (1993). What atmospheric oxygen measurements can tell Us about the global carbon cycle. *Global Biogeochemical Cycles*, *7*(1), 37–67. https://doi.org/10.1029/92GB02733

Krall, K. E., Smith, A. W., Takagaki, N., & Jähne, B. (2019). Air–sea gas exchange at wind speeds up to 85 m s^{-1}. *Ocean Science*, *15*(6), 1783–1799. https://doi.org/10.5194/os-15-1783-2019

Large, W. G., & Pond, S. (1981). Open ocean momentum flux measurements in moderate to strong winds. *Journal of Physical Oceanography*, *11*(3), 324–336. https://doi.org/10.1175/1520-0485(1981)011<0324:oomfmi>2.0.co;2

Lawrence, D. M., Fisher, R. A., Koven, C. D., Oleson, K. W., Swenson, S. C., Bonan, G., et al. (2019). The community land model version 5: Description of new features, benchmarking, and impact of forcing uncertainty. *Journal of Advances in Modeling Earth Systems*, *11*(12), 4245–4287. https://doi.org/10.1029/2018MS001583

Li, C., Huang, J., Ding, L., Liu, X., Han, D., & Huang, J. (2021). Estimation of Oceanic and land carbon sinks based on the Most recent oxygen budget. *Earth's Future*, *9*(7), e2021EF002124. https://doi.org/10.1029/2021ef002124

Li, C., Huang, J., Ding, L., Liu, X., Yu, H., & Huang, J. (2020). Increasing escape of oxygen from oceans under climate change. *Geophysical Research Letters*, *47*(11), e2019GL086345. https://doi.org/10.1029/2019GL086345

Li, H., Wigmosta, M. S., Wu, H., Huang, M., Ke, Y., Coleman, A. M., & Leung, L. R. (2013). A physically based runoff routing model for land surface and Earth system models. *Journal of Hydrometeorology*, *14*(3), 808–828. https://doi.org/10.1175/JHM-D-12-015.1

Liang, J. H., Deutsch, C., McWilliams, J. C., Baschek, B., Sullivan, P. P., & Chiba, D. (2013). Parameterizing bubble-mediated air-sea gas exchange and its effect on ocean ventilation. *Global Biogeochemical Cycles*, *27*(3), 894–905. https://doi.org/10.1002/gbc.20080

Liss, P. S., & Merlivat, L. (1986). *Air-sea gas exchange rates: Introduction and synthesis*. Springer Netherlands. https://doi.org/10.1007/978-94-009-4738-2_5

Long, M. C., Deutsch, C., & Ito, T. (2016). Finding forced trends in Oceanic oxygen. *Global Biogeochemical Cycles*, *30*(2), 381–397. https://doi.org/10.1002/2015GB005310

Lundberg, S. M., Erion, G., Chen, H., DeGrave, A., Prutkin, J. M., Nair, B., et al. (2020). From local explanations to global understanding with explainable AI for trees. *Nature Machine Intelligence*, *2*(1), 56–67. https://doi.org/10.1038/s42256-019-0138-9

Lundberg, S. M., & Lee, S.-I. (2017). A unified approach to interpreting model predictions. In I. Guyon, U. V. Luxburg, S. Bengio, H. Wallach, R. Fergus, S. Vishwanathan, et al. (Eds.), *Advances in neural information processing systems* (Vol. 30). Curran Associates, Inc. Retrieved from https://proceedings.neurips.cc/paper_files/paper/2017/file/8a20a8621978632d76c43dfd28b67767-Paper.pdf

Matear, R. J., Hirst, A. C., & McNeil, B. I. (2000). Changes in dissolved oxygen in the Southern Ocean with climate change. *Geochemistry, Geophysics, Geosystems*, *1*(11). https://doi.org/10.1029/2000GC000086

Moore, J. K., Doney, S. C., & Lindsay, K. (2004). Upper ocean ecosystem dynamics and iron cycling in a global three-dimensional model. *Global Biogeochemical Cycles*, *18*(4), 1–21. https://doi.org/10.1029/2004GB002220

Moore, J. K., Lindsay, K., Doney, S. C., Long, M. C., & Misumi, K. (2013). Marine ecosystem dynamics and biogeochemical cycling in the community earth system model [CESM1(BGC)]: Comparison of the 1990s with the 2090s under the RCP4.5 and RCP8.5 scenarios. *Journal of Climate*, *26*(23), 9291–9312. https://doi.org/10.1175/JCLI-D-12-00566.1

Morgan, E. J., Lavric, J. V., Arévalo-Martínez, D. L., Bange, H. W., Steinhoff, T., Seifert, T., & Heimann, M. (2019). Air–sea fluxes of greenhouse gases and oxygen in the northern Benguela current region during upwelling events. *Biogeosciences*, *16*(20), 4065–4084. https://doi.org/10.5194/bg-16-4065-2019

Najjar, R. G., Jin, X., Louanchi, F., Aumont, O., Caldeira, K., Doney, S. C., et al. (2007). Impact of circulation on export production, dissolved organic matter, and dissolved oxygen in the ocean: Results from phase II of the ocean Carbon-cycle model intercomparison project (OCMIP-2). *Global Biogeochemical Cycles*, *21*(3), 3007. https://doi.org/10.1029/2006GB002857

Nevison, C. D., Manizza, M., Keeling, R. F., Kahru, M., Bopp, L., Dunne, J., et al. (2015). Evaluating the ocean biogeochemical components of Earth system models using atmospheric potential oxygen and ocean color data. *Biogeosciences*, *12*(1), 193–208. https://doi.org/10.5194/bg-12-193-2015

Orr, J. C., Najjar, R. G., Aumont, O., Bopp, L., Bullister, J. L., Danabasoglu, G., et al. (2017). Biogeochemical protocols and diagnostics for the CMIP6 ocean model intercomparison project (OMIP). *Geoscientific Model Development*, *10*(6), 2169–2199. https://doi.org/10.5194/GMD-10-2169-2017

Orsi, A. H., Whitworth, T., & Nowlin, W. D. (1995). On the meridional extent and fronts of the antarctic circumpolar current. *DEEP SEA RESEARCH -PART*, *1*–(5), 641–673. https://doi.org/10.1016/0967-0637(95)00021-W

Oschlies, A. (2021). A committed fourfold increase in ocean oxygen loss. *Nature Communications*, *12*(1), 2307. https://doi.org/10.1038/s41467-021-22584-4

Oschlies, A., Brandt, P., Stramma, L., & Schmidtko, S. (2018). Drivers and mechanisms of ocean deoxygenation. *Nature Geoscience*, *11*(7), 467–473. https://doi.org/10.1038/s41561-018-0152-2

Petsch, S. T. (2013). The global oxygen cycle. In *Treatise on geochemistry* (2nd ed.10, pp. 437–473). https://doi.org/10.1016/B978-0-08-095975-7.00811-1

Reinhard, C. T., Planavsky, N. J., Olson, S. L., Lyons, T. W., & Erwin, D. H. (2016). Earth's oxygen cycle and the evolution of animal life. *Proceedings of the National Academy of Sciences*, *113*(32), 8933–8938. https://doi.org/10.1073/pnas.1521544113

21699291, 2026, 9, Downloaded from https://agupubs.onlinelibrary.wiley.com/doi/10.1029/2026JC024425 by Jianping Huang - Lanzhou University , Wiley Online Library on [12/11/2026]. See the Terms and Conditions (https://onlinelibrary.wiley.com/terms-and-conditions) on Wiley Online Library for rules of use; OA articles are governed by the applicable Creative Commons License

Resplandy, L., Keeling, R. F., Stephens, B. B., Bent, J. D., Jacobson, A., Rödenbeck, C., & Khatiwala, S. (2016). Constraints on Oceanic meridional heat transport from combined measurements of oxygen and carbon. *Climate Dynamics*, *47*(9–10), 3335–3357. https://doi.org/10.1007/S00382-016-3029-3/TABLES/10

Roemmich, D., & Gilson, J. (2009). The 2004–2008 mean and annual cycle of temperature, salinity, and steric height in the global ocean from the argo program. *Progress in Oceanography*, *82*(2), 81–100. https://doi.org/10.1016/j.pocean.2009.03.004

Rustogi, P., Resplandy, L., Bushinsky, S., & Deike, L. (2026). The influence of waves and bubbles on oxygen in the ocean interior. *Environmental Research Letters*, *21*(9), 094001. https://doi.org/10.1088/1748-9326/ae612b

Sallée, J.-B., Shuckburgh, E., Bruneau, N., Meijers, A. J. S., Bracegirdle, T. J., Wang, Z., & Roy, T. (2013). Assessment of Southern Ocean water mass circulation and characteristics in CMIP5 models: Historical bias and forcing response. *Journal of Geophysical Research: Oceans*, *118*(4), 1830–1844. https://doi.org/10.1002/jgrc.20135

Schmidtko, S., Stramma, L., & Visbeck, M. (2017). Decline in global Oceanic oxygen content during the past five decades. *Nature*, *542*(7641), 335–339. https://doi.org/10.1038/nature21399

Stanley, R. H. R., Jenkins, W. J., Lott, D. E., & Doney, S. C. (2009). Noble gas constraints on air-sea gas exchange and bubble fluxes. *Journal of Geophysical Research*, *114*(C11), 2009JC005396. https://doi.org/10.1029/2009JC005396

Stramma, L., Oschlies, A., & Schmidtko, S. (2012). Anticorrelated observed and modeled trends in dissolved Oceanic oxygen over the last 50 years. *Biogeochemistry: Open Ocean*. https://doi.org/10.5194/bgd-9-4595-2012

Sullivan, P. P., Romero, L., McWilliams, J. C., & Melville, W. K. (2012). Transient evolution of langmuir turbulence in ocean boundary layers driven by hurricane winds and waves. *Journal of Physical Oceanography*, *42*(11), 1959–1980. https://doi.org/10.1175/JPO-D-12-025.1

Svein, V., Craig, M. N., & Nadja, & Steiner. (2010). Upper ocean bubble measurements from the NE Pacific and estimates of their role in air-sea gas transfer of the weakly soluble gases nitrogen and oxygen. *Journal of Geophysical Research*. https://doi.org/10.1029/2009JC005990

Talley, L. (2013). Closure of the global overturning circulation through the Indian, Pacific, and southern oceans: Schematics and transports. *Oceanography*, *26*(1), 80–97. https://doi.org/10.5670/oceanog.2013.07

Turner, A. K., & Hunke, E. C. (2015). Impacts of a mushy-layer thermodynamic approach in global sea-ice simulations using the CICE sea-ice model. *Journal of Geophysical Research: Oceans*, *120*(2), 1253–1275. https://doi.org/10.1002/2014JC010358

Wang, Y., Li, C., Huang, J., Ding, L., Liu, X., Han, D., & Huang, N. (2026). Analysis scripts and data for "enhanced Southern Ocean O_2 uptake due to bubble-mediated gas exchange revealed by climate model simulations [Software]. *Zenodo*. https://doi.org/10.5281/ZENODO.19042651

Wanninkhof, R. (1992). Relationship between wind speed and gas exchange over the ocean. *Journal of Geophysical Research*, *97*(C5), 7373–7382. https://doi.org/10.1029/92JC00188

Wanninkhof, R. (2014). Relationship between wind speed and gas exchange over the ocean revisited. *Limnology and Oceanography: Methods*, *12*(JUN), 351–362. https://doi.org/10.4319/lom.2014.12.351

Woolf, D. K. (1997). Bubbles and their role in gas exchange. In P. S. Liss & R. A. Duce (Eds.), *The sea surface and global change* (1st ed., pp. 173–206). Cambridge University Press. https://doi.org/10.1017/CBO9780511525025.007

Yang, B., Emerson, S. R., & Bushinsky, S. M. (2017). Annual net community production in the subtropical Pacific Ocean from in situ oxygen measurements on profiling floats. *Global Biogeochemical Cycles*, *31*(4), 728–744. https://doi.org/10.1002/2016GB005545

21699291, 2026, 9, Downloaded from https://agupubs.onlinelibrary.wiley.com/doi/10.1029/2026JC024425 by Jianping Huang - Lanzhou University , Wiley Online Library on [12/11/2026]. See the Terms and Conditions (https://onlinelibrary.wiley.com/terms-and-conditions) on Wiley Online Library for rules of use; OA articles are governed by the applicable Creative Commons License